Cell Stem Cell

Article

A combined enteric neuron-gastric tumor organoid reveals metabolic vulnerabilities in gastric cancer

Graphical abstract

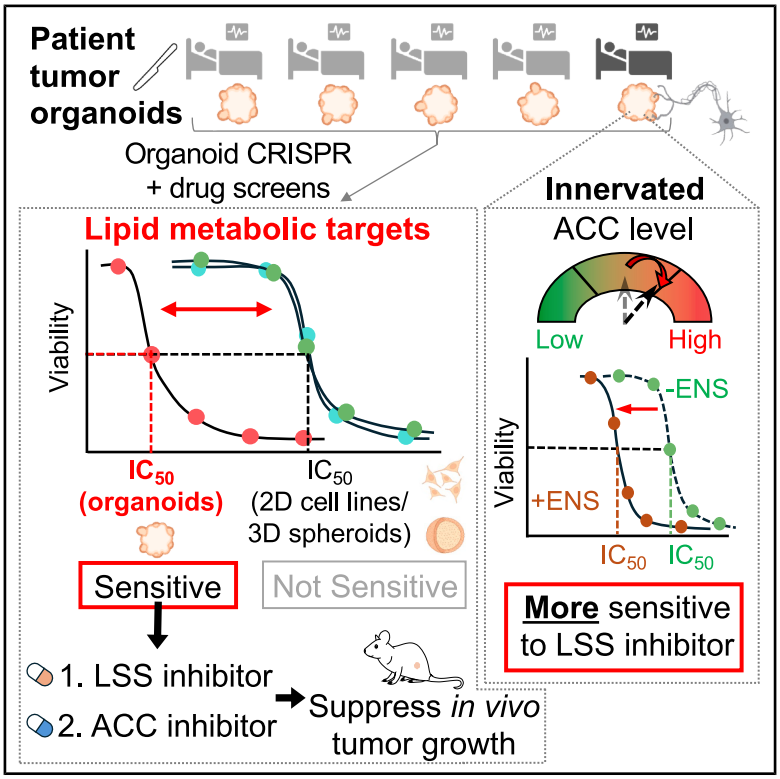

Highlights

- Reprioritization of cancer targets by CRISPR screens with human tumor organoids
- Organoid, not 2D cell or spheroid, mimics *in vivo* tumor's lipid metabolic reliance
- Cholesterol- and fatty-acid-lowering drugs inhibit gastric cancer growth
- Neurons alter cancer cells' lipid metabolism to affect drug responsiveness

Authors

Becky K.C. Chan, Chu Zhang, Chi Him Poon, ..., Helen H.N. Yan, Suet Yi Leung, Alan S.L. Wong

Correspondence

yanhelen@hku.hk (H.H.N.Y.), suetyi@hku.hk (S.Y.L.), aslw@hku.hk (A.S.L.W.)

In brief

Chan and colleagues use CRISPR screens in patient-derived tumor organoids to reveal metabolic vulnerabilities not seen in 2D and 3D spheroid models and identify potent inhibitors that target gastric cancer's lipid metabolism. A neuron-cancer coculture screen found that ACC level predicts treatment efficacy, highlighting neuronal interaction in cancer lipid reliance.

Chan et al., 2025, Cell Stem Cell *32*, 1595–1613
October 2, 2025 © 2025 The Author(s). Published by Elsevier Inc.
https://doi.org/10.1016/j.stem.2025.08.006

CellPress

Cell Stem Cell

CellPress
OPEN ACCESS

Article

A combined enteric neuron-gastric tumor organoid reveals metabolic vulnerabilities in gastric cancer

Becky K.C. Chan,[1,2,5] Chu Zhang,[1,2,5] Chi Him Poon,[1,2,5] Marie H.Y. Lee,[1,2] Hoi Yee Chu,[1,2] Bei Wang,[1,2] Sin-Guang Chen,[1,2] Helen H.N. Yan,[1,3,*] Suet Yi Leung,[1,3,4,*] and Alan S.L. Wong[1,2,6,*]

[1]Centre for Oncology and Immunology, Hong Kong Science Park, Pak Shek Kok, Hong Kong SAR, China
[2]Laboratory of Combinatorial Genetics and Synthetic Biology, School of Biomedical Sciences, The University of Hong Kong, Pokfulam, Hong Kong SAR, China
[3]Department of Pathology, School of Clinical Medicine, The University of Hong Kong, Queen Mary Hospital, Pokfulam, Hong Kong SAR, China
[4]Centre for PanorOmic Sciences, LKS Faculty of Medicine, The University of Hong Kong, Pokfulam, Hong Kong SAR, China
[5]These authors contributed equally
[6]Lead contact
*Correspondence: yanhelen@hku.hk (H.H.N.Y.), suetyi@hku.hk (S.Y.L.), aslw@hku.hk (A.S.L.W.)
https://doi.org/10.1016/j.stem.2025.08.006

SUMMARY

The discrepancy between organoid and immortalized cell line cultures for cancer target discovery remains unclear. Here, our multi-tiered clustered regularly interspaced short palindromic repeats (CRISPR) screens reveal *in vivo*-relevant metabolic dependencies and synthetic lethal pairs that can be uncovered with tumor organoids but not cell lines or even three-dimensional (3D) spheroids. These screens identify lanosterol synthase and acetyl-coenzyme A (CoA) carboxylase inhibitors as effective treatments that impede xenografted tumor growth in mice. These lipid metabolic inhibitors exhibit nanomolar half-maximal inhibitory concentration (IC_{50}) values across diverse human gastric cancer organoids resistant to first-line treatments. Mechanistically, gastric cancer organoids and *in vivo* tumors exhibit lipid metabolic adaptations not seen in two-dimensional (2D) *in vitro* cultures. Additionally, enteric neurons modulate lipid metabolism in tumor organoids, altering drug sensitivity by up to two orders of magnitude. A neuron-cocultured CRISPR screen further reveals that acetyl-CoA carboxylase expression determines lanosterol synthase inhibitor efficacy. These findings highlight the critical roles of organoid environment and neuronal interaction in cancer lipid reliance.

INTRODUCTION

The interaction between cancer cells and the extracellular tumor microenvironment (TME) *in vivo* plays a crucial role in establishing a conducive environment for tumor growth.[1] Neurons and nerve fibers are found within the TME, with emerging evidence suggesting their involvement in the tumorigenesis of various cancer types.[2,3] Despite these findings, our understanding of how extracellular matrix and neurons contribute to the TME and tumor pathogenesis remains fragmented due to limited appropriate models for systematic analysis.

To better mimic the TME, organoid culture utilizing an extracellular matrix offers advantages over traditional two-dimensional (2D) culture to predict patient-specific responses to therapeutic treatments.[4,5] One tempting application involves profiling patient-derived tumor organoids using high-throughput clustered regularly interspaced short palindromic repeats (CRISPR) screening to identify therapeutic vulnerabilities. The Cancer Dependency Map (DepMap) project has initiated genome-wide CRISPR dropout screens in more than a thousand cancer cell lines to uncover essential dependencies.[6,7] A few CRISPR positive selection screens were performed in organoids to identify cells resistant to specific growth supplements.[8–10] In the context of cancer biology, identifying crucial therapeutic targets necessitates CRISPR negative selection (i.e., dropout) screens to pinpoint cells that do not survive post selection. Although some studies have performed CRISPR dropout screens in organoids derived from human induced pluripotent stem cells,[11–13] comprehensive genome-wide screens in patient-derived tumor organoids are limited[14] (Table S1).

Here, we utilized a biobank of patient-derived tumor organoids[15,16] for genome-wide CRISPR dropout screening to identify genetic and therapeutic dependencies. Our screening prioritized lipid metabolic dependencies and revealed *acetyl-CoA carboxylase alpha* (*ACACA*) and *lanosterol synthase (LSS)* as druggable therapeutic targets for gastric cancer (GC). The lipid metabolic dependencies crucial for tumor growth *in vivo* were accurately recapitulated in organoids but not in traditional 2D monolayer or three-dimensional (3D) spheroid cultures of cell lines. By coculturing neurons with tumor organoids, we further observed alterations

This is an open access article under the CC BY license (http://creativecommons.org/licenses/by/4.0/).

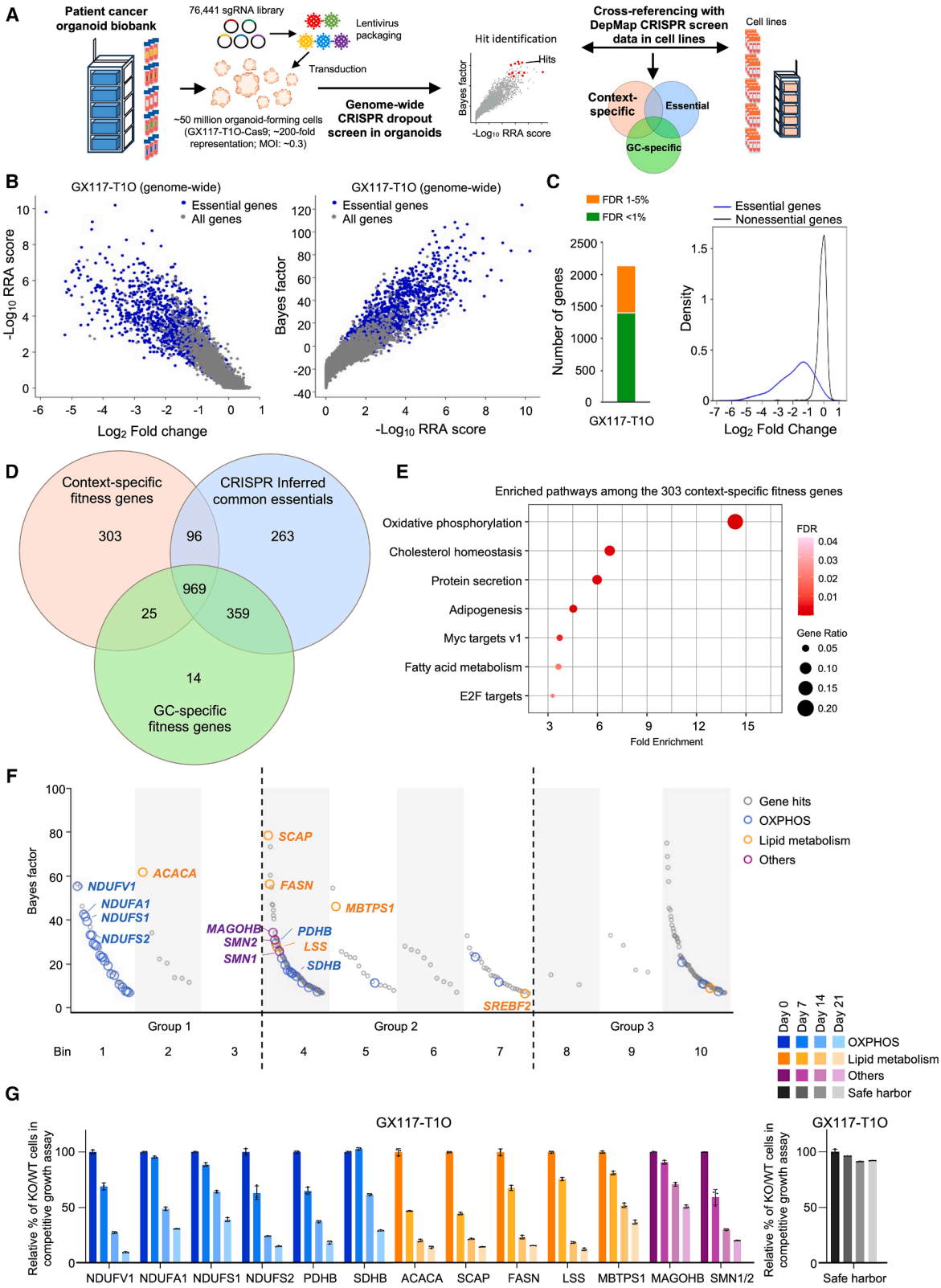

Figure 1. Genome-wide CRISPR dropout screening in patient-derived tumor organoid uncovers context-specific dependencies

(A) Experimental workflow of genome-wide CRISPR dropout screen in patient-derived tumor organoids. To identify context-specific dependencies, organoid-based CRISPR screen hits are compared with those identified from cell-line-based CRISPR screens in Cancer DepMap.

(legend continued on next page)

in the lipid metabolic pathways of GC organoids and changes in their response to specific inhibitors. These findings emphasize the importance of utilizing tumor organoids and considering neuronal influences when selecting key *in vivo* therapeutic targets and agents to optimize treatment outcomes.

RESULTS

CRISPR dropout screening reveals dependencies of patient-derived tumor organoids

We performed an organoid-based genome-wide CRISPR dropout screening to exploit its usefulness in systematically identifying cancer dependencies and actionable therapeutic targets (Figure 1A). We transduced the GX117-T1O organoids (Table S2; see STAR Methods) at a low multiplicity of infection with the CRISPR knockout (Brunello) library[17] consisting of 76,441 single-guide RNAs (sgRNAs) targeting 19,114 genes (Figures S1A and S1B). We applied the model-based analysis of genome-wide CRISPR-Cas9 knockout (MAGeCK)[18] and Bayesian analysis of gene essentiality (BAGEL)[19] analytical pipelines to identify fitness genes and validated the high quality of our screen (Figures 1B, 1C, S1C, and S1D; Table S3; see STAR Methods).

To identify context-specific fitness genes for GX117-T1O, we compared the list of 1,393 depleted genes (with false discovery rate [FDR] cutoff of 1%) from our screen with essential gene lists and filtered out genes that were previously described as essential in cell lines. Because CRISPR-inferred common essential genes were defined based on their fitness values observed in pan-cancer cell lines, we further computed a GC-specific fitness gene list using the fitness data from 33 GC cell lines to cover genes that are essential to GC (see STAR Methods). Our filter isolated 303 gene hits that could be patient- or organoid-specific dependencies or previously undefined essential genes (Figure 1D; Table S3). We then conducted pathway enrichment analysis using the Hallmark gene sets on the 303 gene hits and found that oxidative phosphorylation (OXPHOS) is the most significantly enriched pathway (Figure 1E). The results were further confirmed using three other pathway databases (Figure S1E). We next compared batch-corrected Chronos data of the organoid and the 33 GC cell lines with data published.[22] A more negative Chronos indicated by the left-shifted peak in the organoid was observed in the OXPHOS-related gene sets, particularly for the genes subcategorized as mitochondrial respiratory complex I (Figure S1F), illustrating that the organoid is more vulnerable to the knockouts of complex I subunit genes compared with cell lines. Comparable Chronos data between the organoid and cell lines were observed in the essential gene sets such as G2M checkpoint targets as well as in other gene sets such as allograft rejection that were not fundamental for *in vitro* survival, providing references in the Chronos comparison (Figure S1F). Our results are in line with the idea that OXPHOS dependency is a targetable weakness of cancer cells, particularly for those with stemness features,[23,24] which are present in tumor organoids.

We also assessed the tractability of the 303 gene hits to prioritize potential drug targets and ranked them by Bayes Factor (BF) (Figure 1F; Table S4), with a lower bin number indicating higher tractability[25,26] (see STAR Methods). The OXPHOS genes are grouped in bin 1 (Figure 1F), indicating that they are druggable targets. In addition, we identified a group of gene hits (i.e., *ACACA*, *SCAP*, *FASN*, *LSS*, and *MBTPS1*) comprising key regulators in fatty acid and cholesterol synthesis/lipid metabolism (enriched as "regulation of cholesterol biosynthesis by SREBP" and "cholesterol homeostasis" in the Reactome and Hallmark gene sets, respectively) (Figure S1E), and they are categorized in bins 2–5 and have high BF scores (i.e., from 27.8 to 78.6) (Figure 1F). Most (i.e., 955 out of 1,617) of the known essential genes showed a BF score of >10 (Figure 1B). We also noticed that there are gene hits (*MAGOHB*, *SMN1*, and *SMN2*) categorized in bin 4 that have high BF scores (> 25.8) (Figure 1F) but few literatures describe their potential roles in cancer. The growth inhibitory effects of the gene hit knockouts were validated in GX117-T1O using growth competition assays (Figure 1G), indicating the reliability of our screen.

We speculated that some of the genes among the 303 gene hits could be broadly useful targets for GC. A second CRISPR screen was conducted using sgRNAs targeting the 303 gene hits in a panel of GC organoids (Figures 2A, 2B, and S2A; Data S1A and S1B), comprising five morphologically or molecularly diverse organoids (GX052-TO, GX058-TO, GX068-TO, GX069-TO, and GX076-TO), all with similar doubling times (29.2–43.6 h), to maintain a comparable dropout rate over a 3-week culture period (Table S2). Notably, the common gene hits identified in five or more organoids screened for the context-specific fitness genes consisted of several lipid-metabolism-related genes (including *ACACA*, *FASN*, and *LSS*) (Figures 2B and 2C; Table S5), which were prioritized in the GX117-T1O screen. Growth suppression effects upon knockout of these gene hits were individually confirmed in multiple organoids (i.e., GX058-TO and GX076, which cover mixed subtypes harboring *ARHGAP* fusion and *TP53* mutation, respectively; GX036-TO

(B) The essentiality of each gene in the genome-wide library was analyzed by MAGeCK and BAGEL. A more positive $-\log_{10}$ (robust rank aggregation; RRA) and/or Bayes factor indicates a higher confidence of fitness loss that results from the knockout of a given gene. Log_2 fold change shows the extent of fitness loss from the screen results. Each dot in the plot represents a gene with $\log_2$ transcripts per million (TPM) > −1 in the genome-wide library, and the essential genes defined in DepMap are shown in blue.

(C) Number of gene hits identified with BAGEL FDR < 0.01 (1,393 genes) and FDR between 0.01 and 0.05 (750 genes) (left). Distributions of gold-standard reference sets of essential and non-essential genes[20,21] in the current screen (right).

(D) Venn diagram comparing the depleted genes (BAGEL FDR < 0.01) (peach circle) with the essential gene set defined in DepMap (CRISPR-inferred common essentials) (blue circle) and the customized GC-specific fitness genes (green circle), resulting in 303 GX117-T1O context-specific fitness genes.

(E) Enriched pathways among the 303 context-specific fitness genes using Hallmark gene sets.

(F) Context-specific fitness genes grouped by tractability and ranked by BF score. Potential gene hits are labeled. OXPHOS and lipid metabolic genes defined in the Reactome pathway database are labeled by blue-bordered and orange-bordered circles, respectively, and genes with limited documentation in cancer research are indicated by purple-bordered circles.

(G) Growth competition assay of GX117-T1O with the indicated gene knockouts. $n = 3$.

See also Figure S1 and Tables S1, S2, S3, and S4.

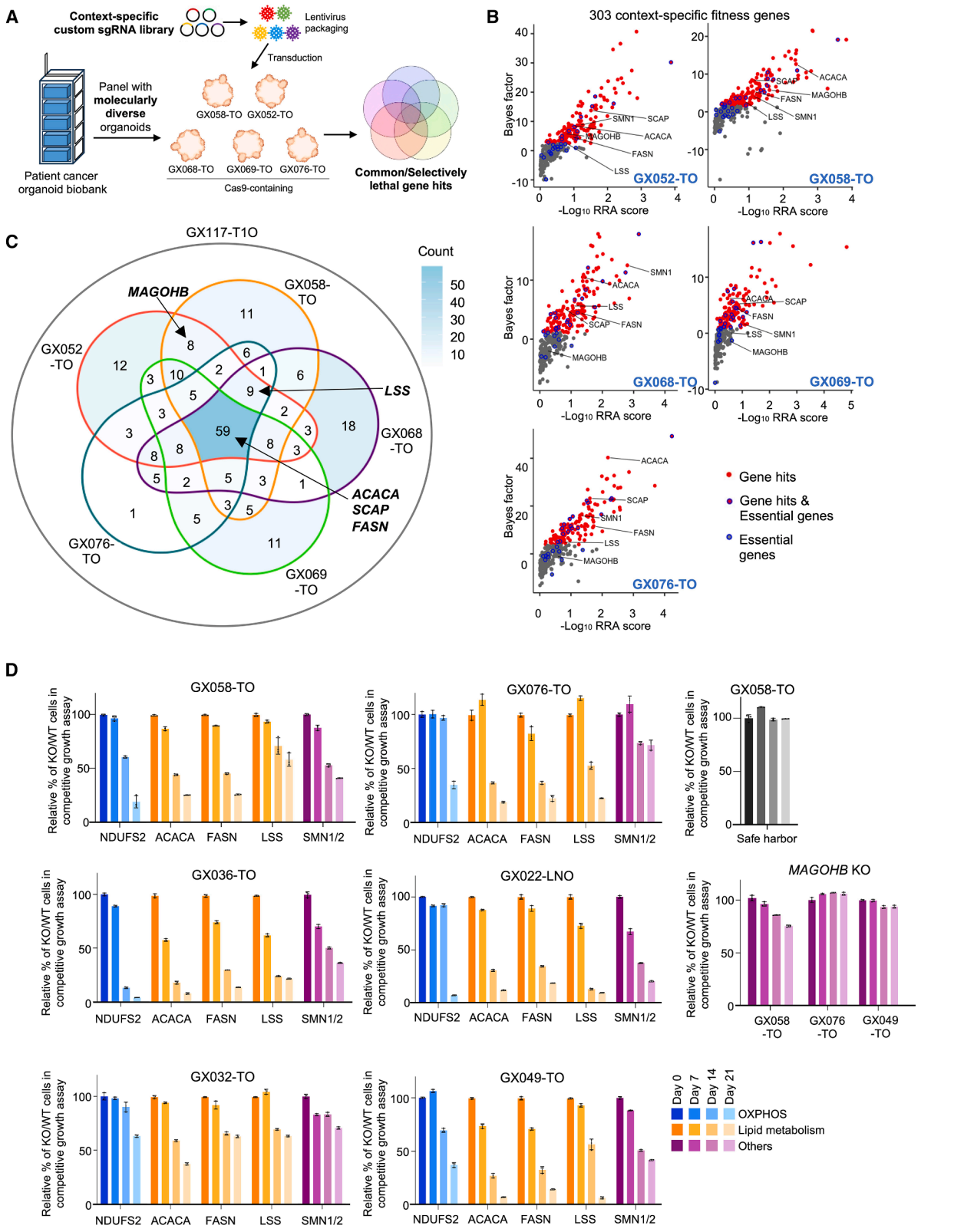

(legend on next page)

and GX022-LNO, covering *CDH1* mutant GC displaying a diffuse growth pattern; and GX032-TO and GX049-TO, covering microsatellite instability[15] [MSI] GC displaying an intestinal growth pattern) (Figures 2D and S2A–S2C; Table S2). These results provide additional confirmation that these targets have the potential to serve as widely applicable targets for GC.

Conversely, *MAGOHB*, a gene involved in RNA splicing and nonsense-mediated messenger RNA decay,[27,28] was consistently identified as a screen hit only in the organoids expressing *ARHGAP* fusion transcripts (Figure 2C; Tables S2 and S5) and was also validated through individual growth competition and mechanistic assays (Figure 2D; details in Data S1). The successful identification and validation of specific target dependencies reinforce the robustness of our screens.

Pharmacological validation of screen hits

Upon validating the influence of gene knockouts on tumor organoids harboring diverse molecular subtypes, we moved on to evaluate their therapeutic potential with corresponding drug inhibitors that are commercially available (Figure 3A). Complex I inhibitors (rotenone, a metformin derivative IM-156, and IACS-010759[29]), acetyl-CoA carboxylase (ACC) (encoded by *ACACA*) inhibitors (ND630[30] and ND646[31]), a FASN inhibitor (TVB-2640),[32] and a *LSS* inhibitor (RO 48-8071), were administered to GX117-T1O. 5-Fluorouracil (5-FU), a first-line drug used for GC treatment, was included to compare drug efficacies. Inhibitors for MAGOHB and SMN1/2 were not available to us and thus were not included in our tests, but they and other screen hits may represent potential therapeutic targets for future drug development and evaluation. All the tested drugs inhibited the GX117-T1O organoid's growth with half-maximal inhibitory concentrations (IC_{50}) ranging from 0.02 to 48.7 μM, as determined by the Genomics of Drugs Sensitivity in Cancer (GDSC) IC_{50} R package (Figure 3B). Among them, the fatty acid and cholesterol synthesis inhibitors ND646 and RO 48-8071 showed the greatest inhibition effects, with IC_{50} values of 0.12 and 0.02 μM, respectively, which are up to 316.9 times lower than the IC_{50} for 5-FU (Figure 3B). Strong growth-suppressive effects were also observed when ND646 and RO 48-8071 were applied to another organoid, GX058-TO (Figure 3B). These results exemplify that translating the genetic hit discovery from organoid CRISPR screen to pharmacological validation can nominate candidate drugs effective for treating the tumors.

Target prioritization and identification of lipid metabolism as tumor-organoid-dependent vulnerability

The more desired therapeutic targets would be the gene products that are required for cell fitness in specific tumor types because of a lower likelihood of inducing toxicity in other tissues while achieving a high anticancer effect with a maximally tolerated dose.[6,33] In this study, we selected *LSS, ACACA*, and *FASN* as prioritized targets to investigate further based on DepMap-reported dependencies (Figure S3A; see STAR Methods). *LSS* encodes lanosterol synthase, which is an essential rate-limiting enzyme in regulating cholesterol biosynthesis. *ACACA* encodes ACC, which controls one of the rate-limiting steps in fatty acid synthesis. *FASN* also encodes a key enzyme in the fatty acid synthesis process. In line with the DepMap data, our individual growth competition assays showed that knockouts of *LSS* and *ACACA* did not affect the growth of four GC cell lines (SNU-1, HGC-27, AGS, and MKN-45) even after up to ~22 rounds of doubling in regular monolayer culture (Figure S3B). Knockout of *FASN* also did not inhibit SNU-1, HGC-27, and AGS cell growth (Figure S3B). In addition, these GC cell lines were much less sensitive to ND646 and RO 48-8071 (with >255-fold and >146-fold higher IC_{50} values, respectively) than GX117-T1O and GX058-TO (Figures 3C and 3D). Conversely, the panel of organoids, which exhibited growth inhibitory effects of the *LSS* and *ACACA* gene knockouts, was sensitive to ND646 and RO 48-8071 treatment, with IC_{50} values ranging from 0.05 to 6.12 μM and 10 to 70 nM, respectively (Figures 3C and 3D). The addition of the exogenous fatty acids, palmitic acid, or oleic acid rescued the growth inhibition of tumor organoids under ND646 treatment (Figures S3C and S3D), further supporting that fatty acid availability is important for their growth. In contrast, the viability of GC cell lines was not affected by adding the exogenous fatty acids, even when cultured in a delipidated medium (Figure S3E).

A previous work reports on the different dependencies for lung cancer cells cultured in a 2D monolayer versus 3D spheroids.[34] We found that culturing the GC cell lines in 3D as spheroids did not sensitize them to the knockouts of *LSS, ACACA*, and *FASN* (Figure S3B) as well as treatment with ND646 and RO 48-8071 (Figures 3C and 3D). These lipid-metabolism-related genes were also found not to be depleted in the screens using 3D spheroids compared with 2D monolayer culture in the previous study.[34] Thus, the growth inhibitory effects observed in tumor organoids may not simply be due to 3D vulnerability. We also attempted to apply the organoid culture method on the GC cell lines (see STAR Methods). We found that such an organoid-like culture method also did not sensitize these cells to ND646 and RO 48-8071 (Figures 3C and 3D), albeit that the 3D structures formed by these cell lines morphologically resemble the organoid architecture (Figure 3E). It is possible that tumor organoid formation is driven by the self-organizing properties of cancer cells that have greater self-renewal and differentiation

Figure 2. Organoid panel-based CRISPR dropout screening with a focused library identifies lipid-metabolism-related genes as potential targets for GC

(A) Experimental outline for the second CRISPR screen using a focused library targeting the 303 gene hits in five molecularly diverse organoids for potential lethal targets identification.

(B) Scatterplots comparing Bayes factor and $-\log_{10}$(RRA) for each screened organoid. Screen hits with BAGEL FDR < 0.01 are shown in red. Prioritized gene hits identified in GX117-T1O genome-wide screen are labeled. Each dot in the plot represents a gene with $\log_2$ TPM > −1 in the focused library, and the essential genes defined in DepMap are represented by blue-bordered dots.

(C) Venn diagram depicting the number of depleted genes (BAGEL FDR < 0.01) among the 5 organoid lines.

(D) Growth competition assay of organoids harboring a range of diverse molecular subtypes with the indicated gene knockouts. $n = 3$.

See also Figure S2. Data S1, and Tables S2 and S5.

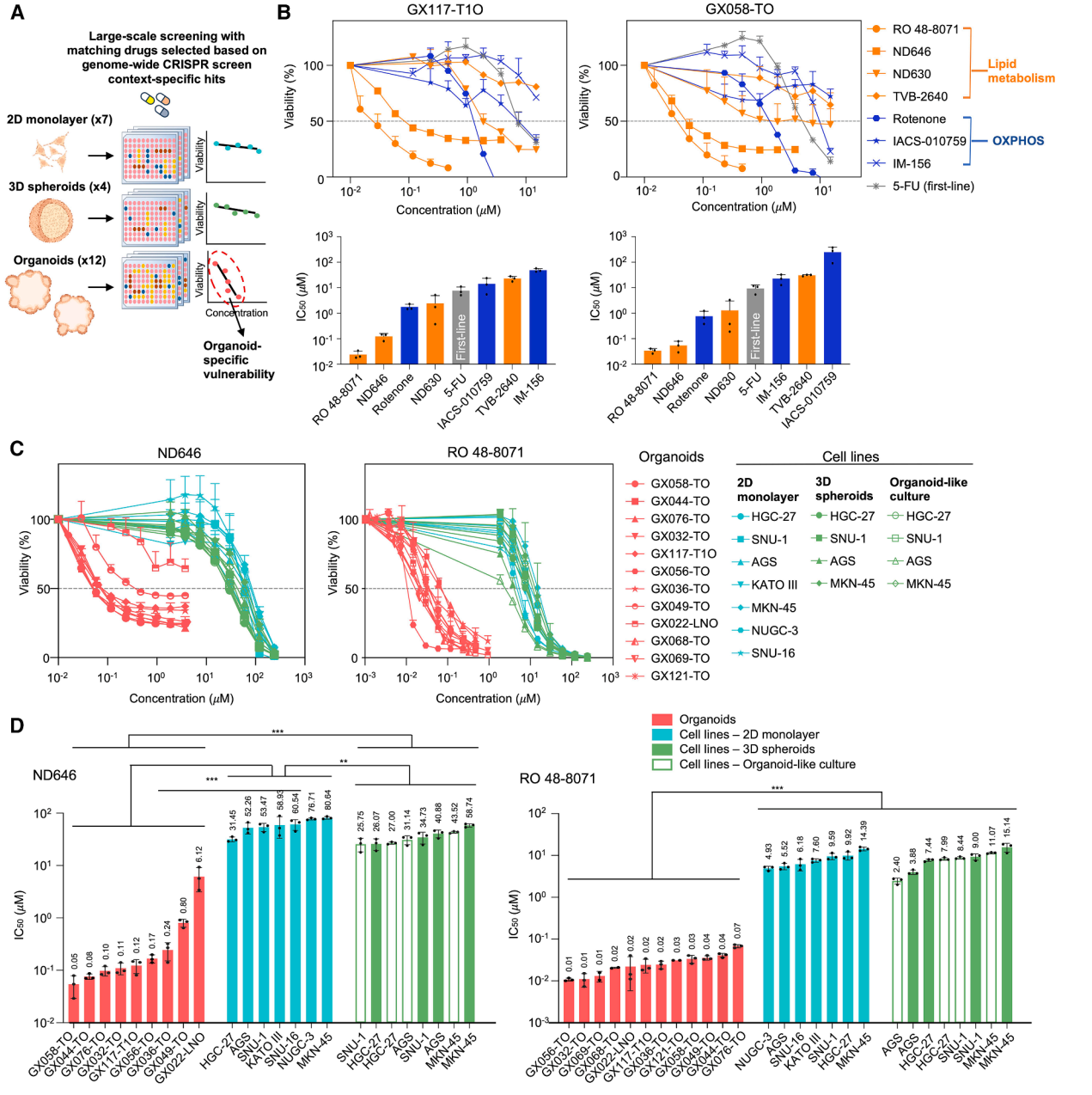

(legend on next page)

capabilities such that multiple physiologically functional cell lineages in the 3D structure may be present.[35,36] As a result, patient-derived tumor organoids could be more physiologically relevant for generating data with greater translational potential *in vivo*.

Taken together, our findings indicate that there are tumor-organoid-dependent vulnerabilities related to fatty acid and cholesterol synthesis that are not identified using cell-line- and spheroid-based studies.

In vivo validation of tumor-organoid-dependent vulnerabilities

The difference between the organoid and cell line results prompted us to test the *in vivo* relevance of the vulnerability identified via tumor-organoid-based CRISPR screening. We attempted to perform an *in vivo* CRISPR dropout assay with a mini, customized pool of sgRNAs targeting the gene hits (*ACACA* and *LSS*, and *NDUFS1*, *NDUFA1*, and *SDHB*, to represent the lipid metabolic and OXPHOS genes, respectively) identified in our organoid CRISPR screens (Figures 4A and S4A–S4C; see STAR Methods). Interestingly, we observed significant depletion of the *ACACA*- and *LSS*- knockout cells *in vivo* but not in the long term 2D culture (Figure 4B). The OXPHOS genes also showed depletion *in vivo* on average, but the extents of depletion were relatively smaller and not statistically significant, considering that large variations were observed among individual animals (Figure 4B). We further looked at The Cancer Genome Atlas (TCGA) dataset and found that high *LSS* expression is associated with inferior overall survival (OS), progression-free survival (PFS), and disease-specific survival (DSS) outcomes of GC (Figure S4D). Besides, high *ACACA* expression predicts unfavorable OS, PFS, and DSS in late-stage GC, although not for early-stage GC (Figure S4D). We thus moved on to further characterize *LSS* and *ACACA* because of their potential clinical relevance. We individually xenografted *ACACA*- and *LSS*-knockout SNU-1 and HGC-27 cells into the mice, confirming significant growth retardation of these cells *in vivo* (Figures 4C–4F). Consistent with the knockout data, mice implanted with GC cells and treated with ND646 or RO 48-8071 displayed pronounced tumor growth inhibition (Figures 4G, 4H, and S4E). The mice did not show signs of behavior abnormalities or significant changes in body weight (Figures 4G, 4H, and S4E), supporting further examination of the use and development of ACC and *LSS* inhibitors for treating GC. Notably, significant tumor suppression was also observed in mice injected with the *ACACA*- and *LSS*-knockout GC organoids, aligning with previous screening and validation data (Figures 4I and S4F). Moreover, upregulation of fatty acid metabolism and cholesterol homeostasis gene expressions were detected in the *in vivo* tumors when compared with the 2D-cultured cells (Figure 5A), which concurs with the higher expressions of these two same pathways in organoids than in 2D-cultured cell lines (Figure 5B). Overall, these results underscore that organoid culture represents a model that better mimics the *in vivo* tumor condition to aid the discovery of dependencies that are relevant *in vivo*.

To substantiate our above observations, we explored the mechanisms underlying the differences in vulnerability toward *ACACA* knockout observed in the 2D culture and *in vivo* conditions. Given the known function of *ACACA* to encode ACC for controlling *de novo* fatty acid synthesis (Figure S4G), we compared the metabolite levels in dummy and *ACACA*-knockout cells that were either cultured in 2D monolayer or collected from the established *in vivo* tumors. We detected a higher level of fatty acids in the *in vivo* tumor when compared with the cells cultured in 2D (Figure 5C). Using mass spectrometric analysis to measure the composition of fatty acids, the *in vivo* tumors were revealed to contain a higher percentage of long-chain fatty acids (i.e., defined in this study as those with C18 or above) than the 2D culture (Figures 5D, 5E, and S5A). In addition, we found that the percentages of C20:4 and C22:6 were reduced in *ACACA*-knockout tumors when compared with the wild-type (WT; i.e., with dummy control) tumors, whereas no obvious difference was detected when comparing WT and *ACACA*-knockout cells cultured in 2D (Figures 5F and S5A). Such discrepancy observed in long-chain fatty acid profiles between *in vitro* and *in vivo* models could be attributed to the observation made by a previous report on the limited access to lipid due to the culture medium and hence the inability to produce sufficient polyunsaturated fatty acids required for the synthesis of long-chain fatty acids in cultured cells.[37] Meanwhile, essential fatty acids (such as linoleic acid) can be obtained through dietary means and contribute to the production of long-chain fatty acids in animal models.[38] Considering the limited ability of *in vitro* models to efficiently elongate long-chain fatty acids such as C20:4 and C22:6, *ACACA*-knockout

Figure 3. Pharmacological validation of screen hits reveals dependencies that are present in tumor organoids but not in the 2D and 3D spheroid cultures of cell lines

(A) Schematic diagram illustrates the workflow to identify effective drug candidates selected based on organoid CRISPR-screen-nominated gene targets. Drug validation results of organoids were compared with those 2D monolayer cell lines (n = 7) and 3D cell line spheroids (n = 4) to confirm organoid-specific vulnerability.

(B) Dose-response curves (upper) and IC_{50} values (lower, determined by the GDSC IC_{50} R package) of GX117-T1O and GX058-TO treated with corresponding drug inhibitors of potential screen hits identified in the genome-wide screening. The dashed line corresponds to 50% viability. n = 3.

(C and D) Dose-response curves (upper) and IC_{50} values (lower) of a panel of organoids and GC cell lines treated with ND646 and RO 48-8071. Cell lines seeded in conventional culture plates, and ultra-low binding plates are grouped as 2D monolayer and 3D spheroids, respectively. Organoid-like culture refers to plating cells in a well coated with a thick layer of BME, adopting a similar drug validation approach as organoids. The dashed line corresponds to 50% viability. n = 3. Data are presented as mean ± SD. Statistical analysis of IC_{50} was performed by Mann-Whitney test. $^{**}p < 0.01$ and $^{***}p < 0.001$.

(E) Schematic diagram illustrating the culture conditions for 2D monolayer, 3D spheroids, organoid-like culture, and organoids. Peach square denotes the presence of culture components in each method. Representative bright-field microscopy images of GC cell lines maintained in 2D monolayer, 3D spheroids, and organoid-like culture using conventional culture dishes, ultra-low attachment plates, and culture plates with a thick layer of BME coating, respectively. Representative microscopy images of organoids with mixed, diffuse, intestinal, and Epstein-Barr virus (EBV)-associated subtypes are shown for comparison. Scale bar, 100 μm.

See also Figure S3.

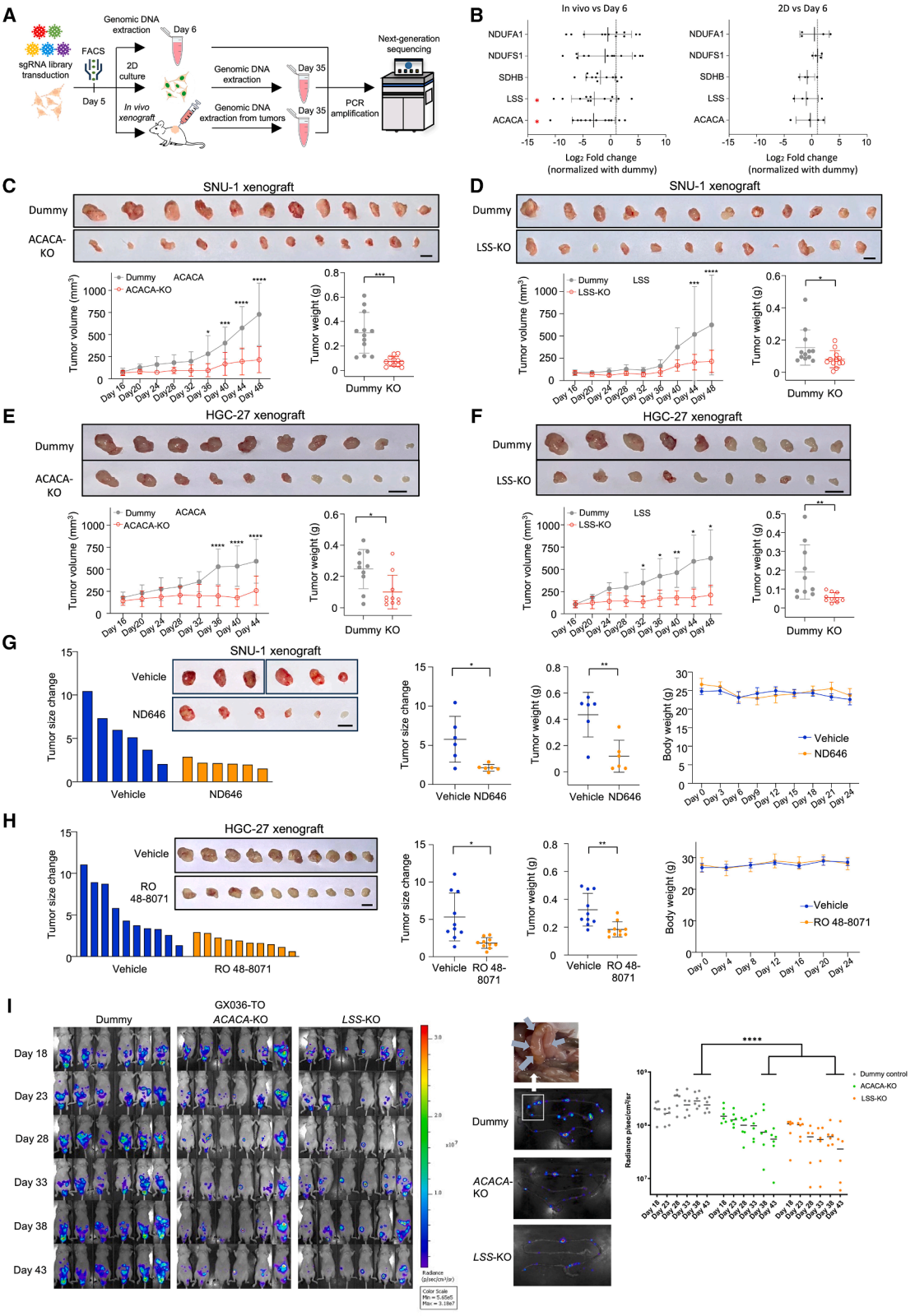

Figure 4. *In vivo* validation of tumor-organoid-dependent vulnerabilities

(A) Experimental workflow of the *in vivo* mini CRISPR dropout assay.

(B) Comparison of $\log_2$ fold change of each sgRNA normalized with non-targeting sgRNAs on day 35 (*in vivo*: left; 2D: right) versus day 6. The dashed line indicates a $\log_2$ fold change of the non-targeting sgRNAs (*in vivo*: $n = 12$, 2 sgRNAs per gene from each of the 6 individual tumors; 2D culture: $n = 4$, 2 sgRNAs per gene from

(legend continued on next page)

organoids exhibited a significant reduction in C18:1 compared with WT control (Figure 5G). To investigate whether these changes were influenced by culture conditions, we analyzed fatty acid compositions in cells cultured on ultra-low binding plates or basement membrane extract (BME)-coated surfaces (Figure S5C). Similar to 2D-cultured cells, knockout of *ACACA* did not significantly alter fatty acid profile in either of the 3D-culturing methods. This is consistent with our analysis of the published CRISPR screening results comparing 2D and 3D cultures of a lung cancer cell line,[34] in which the 2D cell line originally lacking fatty acid dependence did not develop such dependence when cultured as a 3D spheroid (Figure S5D). Collectively, these findings suggest that there is a shift in fatty acid metabolism when transiting from 2D culture to organoid or *in vivo* conditions, and such a shift is *ACACA* dependent. We also measured the levels of other metabolic intermediates in the glycolysis and tricarboxylic acid (TCA) cycle in the same samples. We observed higher percentages of glycerol-3-phosphate (G3P) and glycerol in the WT *in vivo* tumor when compared with the cells cultured in 2D (Figures 5H and S5B), whereas knockout of *ACACA* decreased the ratio of G3P to glycerol in the *in vivo* tumor (Figure 5I). G3P and fatty acids are the building blocks of triglyceride (TG), which stores fatty acids in cells and is important for promoting lipid homeostasis.[39,40] We further showed that the levels of TG (Figure 5J) were increased in tumors compared with 2D-cultured cells, and such an increase was hindered when *ACACA* was knocked out. These results indicate that *ACACA* functions in regulating fatty acid levels and the balance of G3P and glycerol to build TG in GC cells, which may fuel the metabolic adaptation and need for tumor growth *in vivo*. Further work may delineate what specific cues in the *in vivo* environment signal the lipid metabolic shift.

Enteric neurons alter lipid metabolism and drug response of tumor organoids

Perineural invasion is known to correlate with adverse prognosis and unfavorable clinical outcomes in GC and other cancer types.[3] The gastrointestinal tract (GI) encompasses the enteric nervous system (ENS), a distinct intrinsic nervous system that serves as a source of environmental cues to GI cells.[41] GI cancer cells have the ability to adhere to and migrate along ENS neurons,[42] indicating that neurotransmitters and other neuronal secretions may influence tumor progression. Specifically, neurotransmitters present in the TME and vagotomy have been shown to modulate lipid metabolism in GC.[43,44]

Here, we investigated the potential impact of ENS neurons on GC organoids using two coculture methods (Figure 6A). The direct coculture method involved embedding human embryonic stem cell (hESC)-derived enteric neural crest cells (ENCCs) with GC organoids in BME (Figure S6A). The differentiation of ENCCs, characterized by observed neurite extension, was evident by day 2, and then the formation of neuron clusters and extensive neurite innervation were detected by day 7 (Figure S6B). Although some contacts between the GC organoids and neurons were observed under microscopy, only few direct cell-cell interactions were detected using the GFP-based touching nexus (G-baToN)[45] reporter system (Figure S6C). The indirect coculture method involved the terminal differentiation of enteric neurons (ENs) from ENCCs and the collection of its conditioned medium for culturing GC organoids (Figure S6D). Relative gene expressions were compared among the hESC, ENCC, and EN populations, and we confirmed the identity and maturity of the neuronal cultures utilizing a panel of differentiation and neural markers (Figures S6E–S6G; see STAR Methods). RNA sequencing (RNA-seq) was next conducted to assess the impact of cocultures on gene expression in GC organoids. Differentially expressed genes were associated with various pathways, including cholesterol homeostasis, hypoxia, and tumor necrosis factor alpha (TNF-α) signaling, which were upregulated in both direct and indirect ENS cocultures with GX117-T1O organoid (Figure 6B). Genes related to fatty acid metabolism, including *ACACA*, also showed increased expression levels (Figure 6B; Table S6). Similar pathways and gene sets were upregulated when another organoid, GX049-TO, was utilized in the coculture (Figure 6C), suggesting that the neuronal effects may be common across different organoids.

The observed changes in lipid-metabolism-related pathways led us to investigate the influence of neurons on the organoids' drug response to ND646 and RO 48-8071. Our findings revealed a 3.1-fold increase (from 0.13 to 0.40 μM) and a 207.1-fold increase (from 0.018 to 3.727 μM) in the IC_{50} values of ND646 when GX117-T1O and GX049-TO were subjected to the indirect ENS coculture, respectively (Figure 6D). This resistance could be attributed, at least in part, to the increased expression of ACC

each of the 2 biological replicates). Statistical analysis was performed by one-way ANOVA, followed by pairwise comparison-adjusted with the least significant difference. * Denotes the significant difference between the knockout group and non-targeting control in the respective group.

(C and D) Images of resected tumors formed by subcutaneously injected SNU-1 cells infected with a dummy sgRNA or a sgRNA targeting *ACACA* (C) or *LSS* (D) into mice. The growth in tumor volume and the weights of tumors at the endpoint are shown. Scale bar, 1 cm. $n = 12$ per group.

(E and F) Images of resected tumors formed by subcutaneously injected HGC-27 cells infected with a dummy sgRNA or a sgRNA targeting *ACACA* (E) or *LSS* (F) into mice. The growth in tumor volume and the weights of tumors at the endpoint are shown. Scale bar, 1 cm. $n = 10$ per group.

(G) Images of resected tumors in mice subcutaneously injected with SNU-1 cells after treatment with vehicle or ND646 at 12.5 mg/kg BID. Three oversized tumors (left box) in the vehicle-treated group were harvested on day 18 (i.e., 6 days before the endpoint) for animal welfare. Tumor size changes, body weight, and tumor weight at the endpoint are shown. Scale bar, 1 cm. $n = 6$ per treatment group.

(H) Images of resected tumors in mice subcutaneously injected with HGC-27 cells after treatment with vehicle or 40 mg/kg RO 48-8071 QD. Tumor size changes, body weight, and tumor weight at endpoint are shown. Scale bar, 1 cm. $n = 10$ per treatment group.

(I) Images of mice intraperitoneally injected with luciferase-labeled GX036-TO organoids infected with a dummy sgRNA or a sgRNA targeting *ACACA* or *LSS*. The growth in tumor volume is represented as bioluminescence intensity (photons/sec/cm^2/sr) and quantified. $n = 6$ per group. Representative photos of tumor nodules dissected out from the peritoneal cavities of the mice (sacrificed at day 43) are shown.

Data are presented as mean ± SD. Statistical significance in tumor volume and bioluminescence intensity was evaluated by two-way ANOVA with Šidák's post hoc test (C)–(F) and (I). Tumor weight and tumor size change were statistically analyzed by Student's t test (C)–(H). $^{*}p < 0.05$, $^{**}p < 0.01$, $^{***}p < 0.001$, and $^{****}p < 0.0001$.

See also Figure S4.

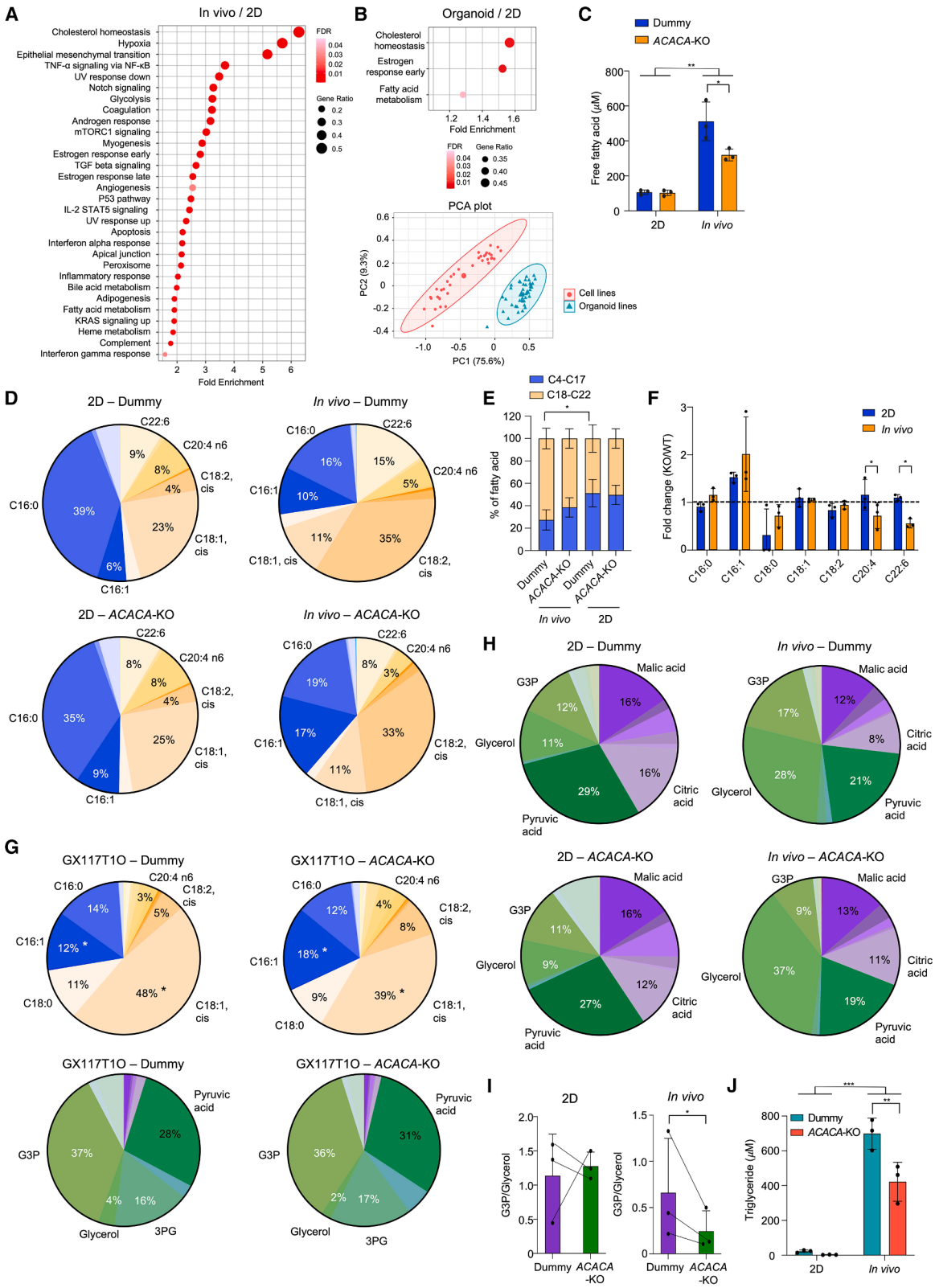

Figure 5. Metabolic adaptation induced by the switch from 2D culture to *in vivo* creates a shift in lipid metabolism

(A) Enriched pathways of the upregulated genes in *in vivo* tumors compared with 2D-cultured SNU-1 cells with reference to Hallmark gene sets. $n = 2$.

(B) Enriched pathways of the upregulated genes in 43 patient-derived GC organoids compared with 37 GC cell lines with reference to Hallmark gene sets (upper). Principal-component analysis (PCA) was performed on the expression profile of the same panel of organoids and cell lines (lower).

(legend continued on next page)

following the coculture (Figure 6E). In contrast, the coculture amplified the sensitivity of GX117-T1O and GX049-TO to RO 48-8071, leading to a 1.5-fold (from 16 to 11 nM) and 6.3-fold (from 38 to 6 nM) decrease in its IC_{50} values, respectively (Figure 6D). Similar results were observed when the organoids were exposed to hypoxic conditions (Figure S7A), indicating that the neuronal effects also apply in this environment. Of note, the neuron coculture did not impact the growth of GC organoids in the absence of the drug treatment (Figure S7B) nor did it affect drug responses when cell lines were utilized (Figure S7C).

To investigate the mechanism through which neurons enhance RO 48-8071 sensitivity, we conducted a CRISPR screening on the commonly upregulated genes identified in the two coculture systems (Figure 6F; see STAR Methods). The indirect coculture method was utilized in this pooled CRISPR screening setup to minimize the variability arising from random direct contact between the neurons and the GC organoids. Our screening revealed that *ACACA* plays a crucial role, as its knockout led to GX049-TO's resistance to RO 48-8071 in the coculture system (Figure 6G; Table S7). Subsequent individual validation assays confirmed this effect (Figure 6H), indicating the dependency of the RO 48-8071 response on *ACACA* expression. Previous studies have shown that *LSS* inhibitors activate a shunt pathway that generates 24(s),25-epoxycholesterol and triggers the activation of sterol regulatory element-binding protein 1 (SREBP1),[46,47] a transcription factor that regulates genes involved in fatty acid biosynthesis, including *ACACA*. SREBP1 activation can result in the accumulation of very long-chain fatty acids and necroptosis,[48,49] and this process depends on fatty acid biosynthesis[50] (Figure S4G). Consistent with these findings, elevated levels of SREBP1 and a further increase in ACC were observed in GC organoids following treatment with RO 48-8071 in the indirect ENS coculture, as well as MLKL phosphorylation, a marker for necroptosis, was evident in GC organoids treated with the drug (Figure 6E), suggesting a similar downstream mechanism was triggered. We also attempted to look into what upstream factors secreted from the ENS neurons contribute to the enhanced RO 48-8071's sensitivity. We speculated that acetylcholine secreted from the neurons might be hydrolyzed by the cancer receiver cells into acetate and choline using acetylcholinesterase, with acetate then being taken up and converted into acetyl-CoA in cancer cells for lipid metabolism. However, we did not observe that acetylcholine treatment affects the GC organoids' sensitivity to RO 48-8071 (Figure S7D), while acetate only slightly lowered its IC_{50} toward RO 48-8071 (Figure S7E). To better mimic the effect of ENS coculture, seven molecules commonly reported to be secreted by ENS, including serotonin, γ-aminobutyric acid (GABA), dopamine, vasoactive intestinal peptide (VIP), neuropeptide Y, substance P, and TNF-α, were administered in three dosage combinations (low, mid, and high; see STAR Methods). ENS secretome at mid dosage combination resulted in lowered IC_{50} toward RO 48-8071 without inducing toxicity in the GC organoid (Figures S7F and S7G). Interestingly, we did not observe that these secretome molecules affect the GC organoids' sensitivity to RO 48-8071 when administered separately (Figure S7H). These results suggested a combined effect from molecules present in the ENS secretome, rather than an individual element, that modulates the response of the GC organoid to RO 48-8071, corroborating the complexity of neuron-cancer crosstalk. Additional research will be required to elucidate the necessary elements from neurons that induce the change to a certain drug response in cancer.

Notably, the association between *ACACA* expression and the response of GC tumors to RO 48-8071 suggests its potential as a biomarker for stratifying tumor responses. Upon further examination of our data across more GC-patient-derived tumor organoids, we noted that those with higher *ACACA* expression exhibited lower IC_{50} values (Pearson's correlation = 0.71) (Figure 6I). Utilizing RO 48-8071 or other *LSS* inhibitors may offer a more efficacious therapeutic strategy than using ACC inhibitors for treating those tumors, particularly in cases with increased innervation that could further augment *ACACA* expression (Figure 7).

DISCUSSION

Our organoid-based CRISPR screening findings, validated in xenografts *in vivo* and a wider range of GC tumor organoids resistant to 5-FU treatment,[15] showed that GC depends on fatty acid and cholesterol synthesis and responds well to the ACC inhibitor ND646 and the *LSS* inhibitor RO 48-8071. The ACC inhibitor has been tested in human clinical trials for type 2 diabetes[51] and nonalcoholic fatty liver disease[52,53] and is generally safe and well-tolerated, albeit that it could result in an asymptomatic reduction in platelet production.[54] There are preclinical tests on using ACC inhibitors for treating hepatocellular carcinoma[55] and non-small cell lung cancer.[31] Further development in directing ACC inhibitors to the stomach—for example, using a bilayer floating capsule[56]—may enhance the safety profile for its potential use in GC treatment. On the other hand, *LSS* is a previously undescribed target for GC. The *LSS* inhibitor RO 48-8071 was shown

(C) Free fatty acid concentration of HGC-27 cells and *in vivo* tumors with dummy and *ACACA* knockouts. $n = 3$.
(D–F) Pie charts depicting the composition of fatty acids in SNU-1 cells and *in vivo* tumors with dummy and *ACACA* knockouts (D). Distribution of short-/medium- (i.e., C4-C17) and long-chain (i.e., C18-C22) fatty acids in SNU-1 cells and *in vivo* tumors with dummy and *ACACA* knockouts (E). Fold change of fatty acid percentage of *ACACA* knockouts (KO) and dummy (WT) in SNU-1 cells and *in vivo* tumors (F). Only fatty acids with high abundance are shown. The dashed line indicates the same level of abundance between dummy and *ACACA* knockouts. $n = 3$.
(G) Pie charts depicting the composition of fatty acids (upper) and glycolysis/TCA cycle intermediates (lower) in GX117-T1O with dummy and *ACACA* KO. $n = 3$ in upper panel; $n = 2$ in lower panel. Statistical significance in fatty acid compositions was statistically analyzed by Student's t test. $^{*}p < 0.05$.
(H and I) Pie charts depicting the composition of glycolysis/TCA cycle intermediates in SNU-1 cells and *in vivo* tumors with dummy and *ACACA* KO (H). Quantification of the G3P-to-glycerol ratio is shown in (I). $n = 3$.
(J) Triglyceride concentration of HGC-27 cells and *in vivo* tumors with dummy and *ACACA* KO. $n = 3$.
Data are presented as mean ± SD. Statistical analysis was performed by two-way ANOVA with Tukey's post hoc test (C), (E), and (I), paired t test (F), or ratio paired t test (H). $^{*}p < 0.05$, $^{**}p < 0.01$, and $^{***}p<0.001$.
See also Figure S5 and Methods S2.

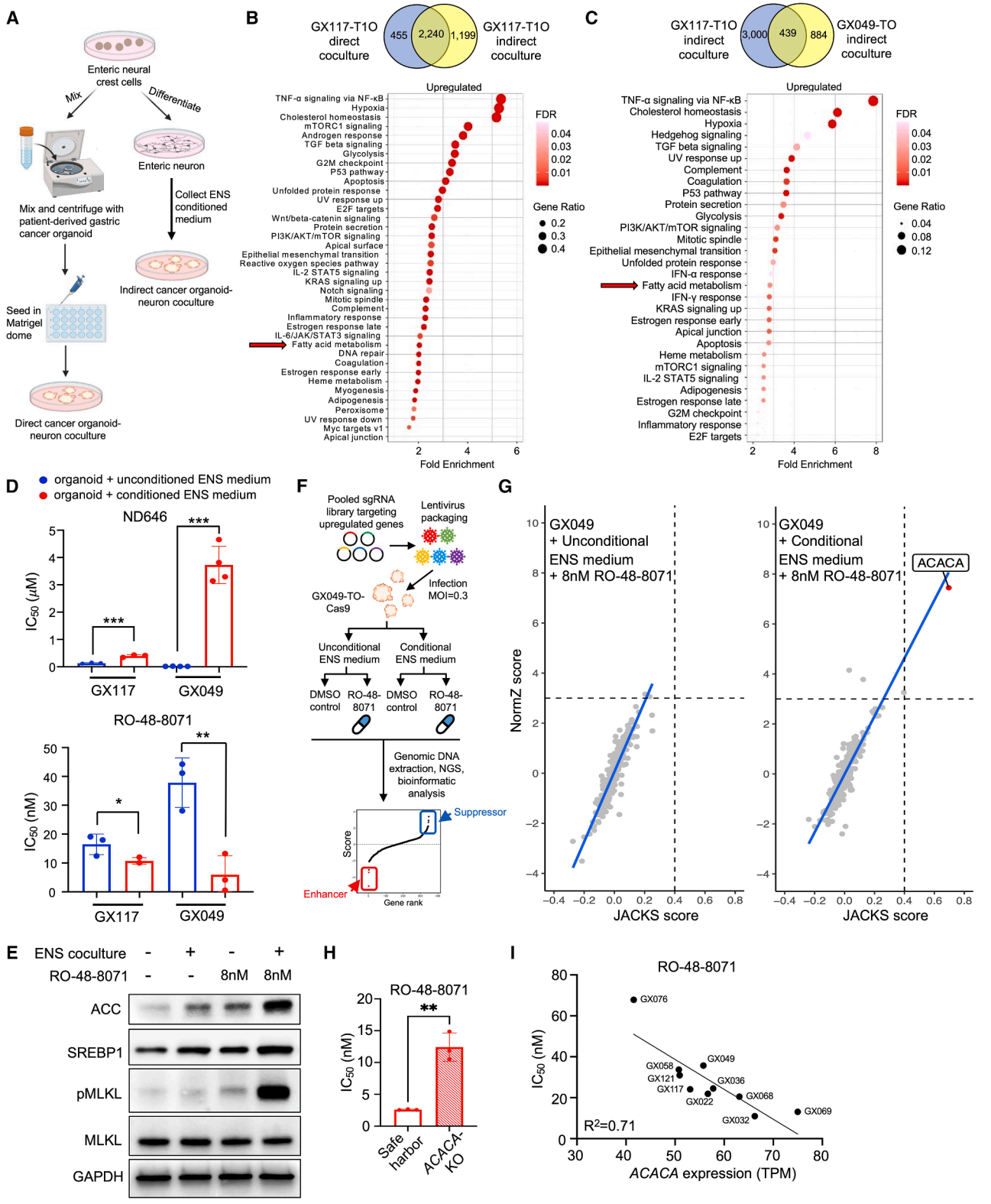

Figure 6. CRISPR screening performed in the presence of enteric neuron secretome reveals that RO 48-8071 sensitivity is dependent on *ACACA*

(A) Schematic diagram illustrates the procedures for generating the GC organoid-ENS coculture model. ENCCs were either combined with organoids through centrifugation and embedded in a BME dome for direct coculture or differentiated into enteric neurons for conditioned medium collection.

(legend continued on next page)

to be safe and effective when applied in squirrel monkeys and mini-pigs as cholesterol-lowering therapy.[57] The dose of RO 48-8071 used in our xenograft studies to achieve a strong anti-cancer effect in mice was lower than its pharmacologically active doses used in the squirrel monkeys and mini-pigs, based on the equivalent dose translation using the body surface area normalization method.[58] RO 48-8071 may represent another drug candidate to be tested and further developed for GC.

The increased reliance on fatty acid and cholesterol synthesis observed in GC organoids and *in vivo* is likely dictated by the intricate biochemical and physical cues present in the TME.[59,60] We speculate that there could be a metabolic shift due to hypoxia-induced metabolic reprogramming in which the 3D architecture of organoids and *in vivo* tumors favors the development of a hypoxic core and a normoxic outer cell layer. Under a hypoxic environment, metabolic reprogramming in cancer cells can be achieved by expressing more hypoxia-inducible factors, which drive the expression of enzymes involved in fatty acid metabolism, such as *FASN*, *ACACA*, and *SCD*.[61–63] Indeed, *SCD* mediates the generation of long-chain fatty acids in GC organoids, contributing to its metabolic rewiring from glycolysis to fatty acid metabolism,[64] which may complement the findings in this study. Differences in the methodologies used in 2D cell line culture and 3D organoid culture may also potentially lead to such a discrepancy, as the addition of BME in organoid culture may introduce a higher degree of stiffness to the microenvironment, which facilitates lipid droplet accumulation.[65] Further mechanistic studies will be required to delineate the actions of key enzymes in this metabolic shift and their clinical significance. Interestingly, our work revealed a previously undescribed role of neurons in modulating cancer's lipid metabolism and the associated drug responses. Furthermore, the expression of *ACACA* could serve as a valuable biomarker for stratifying drug responses and guiding therapeutic choices. Our results shed light on the feasibility of utilizing *ACACA* expression in clinical patient tumor samples to facilitate the decision of therapeutic regimen. Although *ACACA* and *LSS* were both identified as organoid-specific dependencies in our GC-only screening, our ENS-GC organoid coculture system revealed potential confounding effects among these screened hits, suggesting cautions in the usage of combined drugs targeting these dependencies to treat GC effectively. Screening with a broader organoid panel encompassing diverse genomic alterations from various GC patients will help to assess whether specific cancer mutations impact the sensitivity of the cancer cells to these metabolic demands.

There is an unmet need to uncover the dependencies of many cancer subtypes observed in patients. In the DepMap project, tens of available cell lines have been screened for each cancer type to prioritize cancer-type-specific drug targets and suggest new targets.[6,7] However, these only represent a small subset of cancer subtypes and genotypes observed in patients. Many cancers with different individual driver mutations and their combinations, as well as the less common genotypes that encompass about 25% of all cancers, are underrepresented in cell line models.[66] Through the expansion of CRISPR screening to a panel of GC organoids, our study showcases its effectiveness in identifying potential synthetic lethal targets, such as *MAGOHB*, for a common GC subtype characterized by *ARHGAP* gene fusion. Recent efforts in enhancing the feasibility of high-throughput screening gave rise to the development of a suspension technique for organoid culture, allowing procedural simplification while maintaining genotypes and phenotypes.[67] This approach may facilitate a more efficient screening process.

There is a growing collection of clinically and genomically annotated tumor organoids representing various cancer subtypes, such as gastric,[15,16] colon,[68,69] and breast[70,71] cancers, among others. Our study sets the stage for expanding the DepMap project to carry out extensive CRISPR screening on a wide range of tumor organoids representing various cancer types, including numerous unexplored tumor subtypes with diverse mutations. Advances in the CRISPR screening toolbox, including the development of an optimized minimal genome-wide sgRNA library,[72] will also accelerate the progress to perform large-scale organoid CRISPR screens. Base and prime editors[73] can be used to create isogenic tumor organoids to identify synthetic lethal targets. Combinatorial CRISPR screens can be applied to isolate actionable therapeutic combinations.[74–77] To inform how

(B) GC organoids with direct and indirect ENS coculture were analyzed by RNA-seq. Significantly upregulated genes identified by $\log_2$ fold change > 0.4 under direct and indirect coculture are visualized in the Venn diagram, and the common upregulated genes (n = 2,240) were subjected to gene ontology. Enriched pathways detected from common upregulated genes with reference to Hallmark gene sets are shown in the dot plot. n = 2. The red arrow indicates fatty acid metabolism as a significantly enriched gene set, and *ACACA* is among those upregulated genes (see Table S6).
(C) Organoids of mixed (GX117-T1O) and MSI subtype (GX049-TO) were subjected to indirect ENS coculture. Venn diagram depicts the commonly upregulated genes identified by $\log_2$ fold change > 0.4 (n = 439) and their enriched pathways with reference to Hallmark gene sets. n = 2. The red arrow indicates fatty acid metabolism as a significantly enriched gene set, and *ACACA* is among those upregulated genes (see Table S6).
(D) Organoids under indirect ENS coculture exhibited resistance toward ND646 (GX117-T1O, n = 3; GX049-TO, n = 4), whereas conditioned ENS medium sensitized organoids to the effect of RO 48-8071 (GX117-T1O, n = 3; GX049-TO, n = 3).
(E) Treatment of RO 48-8071 induces protein expressions related to fatty acid biosynthesis and necroptosis.
(F) Schematic diagram illustrates the workflow of the CRISPR screen in GC organoid-ENS cocultures.
(G) Selection of gene hits that confer RO 48-8071 resistance to GC organoid under indirect ENS coculture. DrugZ-calculated NormZ score is plotted against joint analysis of CRISPR-Cas9 knockout screens (JACKS) essentiality score. A more positive NormZ score indicates a stronger resistance to the drug conferred by a gene knockout. A higher JACKS essentiality score is associated with a lower gene essentiality.
(H) GX049-TO infected with sgRNA targeting *ACACA* under indirect ENS coculture exhibits a higher IC_{50} value for RO 48-8071. n = 3.
(I) IC_{50} values obtained from GC organoids treated with RO 48-8071 are plotted against their respective *ACACA* expressions in TPM. An inverse correlation indicates the potential role of *ACACA* in mediating the antiproliferative effect of RO 48-8071.
Data are presented as mean ± SD. Statistical analysis of IC_{50} was performed by Student's t test compared with unconditioned ENS medium control (D) or safe harbor knockout control (H). $^*p < 0.05$, $^{**}p < 0.01$, and $^{***}p < 0.001$.
See also Figures S6 and S7 and Tables S6 and S7.

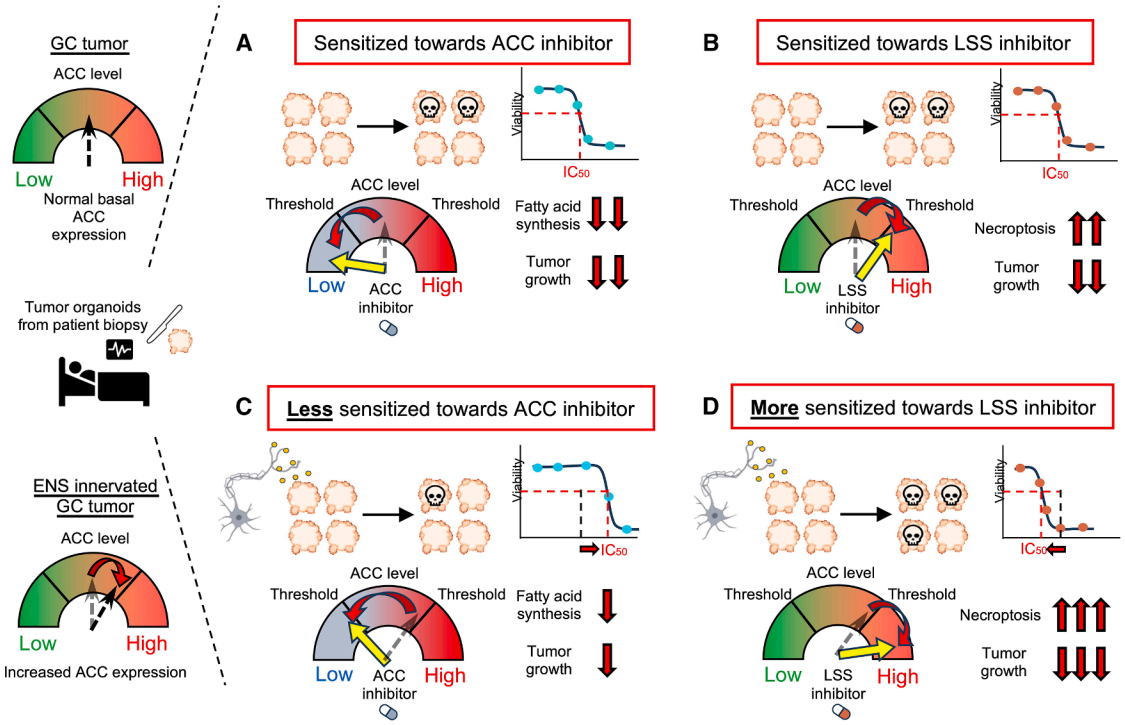

Figure 7. ACC level as a biomarker for treatment stratification to devise a more precise regimen based on tumor types and achieve optimal therapeutic prospects

Tumor organoids from biopsy can be used to categorize patients based on their tumor ACC levels, followed by the therapy determination (ACC inhibitor or *LSS* inhibitor). Growth of tumor can be effectively suppressed by ACC and *LSS* inhibitors through reducing fatty acid synthesis and inducing necroptosis, respectively (A) and (B). However, the effect of these two inhibitors is modulated by the presence of ENS, which reprograms the tumor's lipid metabolism. ENS-innervated tumors are more resistant to ACC inhibitors, which may be potentially mediated by the increased tumor ACC level counteracting the drug's effect (C). In contrast, an increased ACC level sensitizes the tumor to necroptosis induced by *LSS* inhibitor, leading to its stronger anticancer effect in ENS-innervated tumors (D). This framework suggests the possibility of utilizing the ACC level as a biomarker for cancer treatment stratification.

dependencies may change along the tumor evolution, CRISPR screens can also be applied on tumor organoids derived from the same patient at different disease stages, with or without drug treatment, or upon recurrence and metastasis.

Limitations of the study

Future studies should be performed to delineate the specific cues in the TME contributing to the observed metabolic shift from 2D cancer cell culture to organoid and *in vivo* conditions. Although we established that such a shift is *ACACA* dependent, it remains elusive how *ACACA* interacts with the signals from the TME in organoids and *in vivo* to achieve their distinct lipid and fatty acid profiles. The current study employs a neuron-organoid coculture system to assess specific genetic vulnerabilities of GC under the influence of neuronal secretome. Despite promising results in identifying ACACA's potential as a biomarker that may help guide therapeutic options, our indirect coculture model limits the evaluation of neuron-mediated changes in GC organoids to its secretome alone without considering the significance of neuron-cancer physical contacts, which could also contribute to metabolic shift in cancer.[78] Moreover, the effects and concentrations of the secreted factors acting on the tumor largely depend on the nerve's proximity to cells inside an innervated tumor, resulting in heterogeneity in cancer's response to these nerves that is challenging to measure. Further studies using tracing techniques that enable labeling of cancer cells in contact with neurons could be performed to interrogate differences in metabolic patterns between cancer cells with and without neuron innervation.

RESOURCE AVAILABILITY

Lead contact

Further information and requests for resources and reagents should be directed to, and will be fulfilled by, the lead contact, Alan S.L. Wong (aslw@hku.hk).

Materials availability

Recombinant DNA constructs generated as part of this study are available upon reasonable request with a materials transfer agreement (MTA).

Data and code availability

RNA-seq data used in this study are available at Gene Expression Omnibus (GEO) with the following accession number: GEO: GSE303453. Data S1 generated from this study are available at Mendeley data with the following DOI: https://doi.org/10.17632/8xh8sx232r.1. Data reported in this paper are available in Tables S1, S2, S3, S4, S5, S6, and S7 and additional information will be shared by the lead contact upon request. This paper does not report original code.

ACKNOWLEDGMENTS

We thank Kylie H.M. Mak, Yin Kau Lam, Peng Zhou, Gigi C.G. Choi, Dessy Chan, Yin Tong, and Do Kyung Leem for the technical assistance and input.

We thank the Centre for PanorOmic Sciences at LKS Faculty of Medicine, The University of Hong Kong, for providing support on the next-generation sequencing experiments, flow cytometry analysis, and metabolomics analysis. This work was primarily supported by the Centre for Oncology and Immunology Limited under the Health@InnoHK Initiative funded by the Innovation and Technology Commission, The Government of Hong Kong SAR, China, and, in part, by the Research Grants Council of the Hong Kong SAR, China (grant numbers T12-710/16-R and YCRG-C7004-22Y), and the internal fund from the University of Hong Kong (grant number 109002147).

AUTHOR CONTRIBUTIONS

B.K.C.C., C.Z., C.H.P., H.H.N.Y., S.Y.L., and A.S.L.W. conceived the work. H. H.N.Y., S.Y.L., and A.S.L.W. obtained funding. B.K.C.C., C.Z., and C.H.P. designed and performed the experiments and interpreted and analyzed the data. M.H.Y.L., B.W., and S.-G.C. provided technical support for the cell/organoid culture and molecular biology experiments. H.H.N.Y. and S.Y.L. shared expertise on organoid culture and gastric cancer. H.Y.C. provided support for the computational analyses. B.K.C.C. and A.S.L.W. wrote the paper with assistance from all authors.

DECLARATION OF INTERESTS

A.S.L.W., S.Y.L., H.H.N.Y., B.K.C.C., C.Z., and C.H.P. have filed a patent application related to this work. S.Y.L. has received research sponsorships from Pfizer, Merck, and Servier. A.S.L.W. and S.Y.L. are members of *Cell Systems*' and *Cell Stem Cells*' advisory boards, respectively.

STAR★METHODS

Detailed methods are provided in the online version of this paper and include the following:

- KEY RESOURCES TABLE
- EXPERIMENTAL MODEL AND SUBJECT DETAILS
  - Human material for organoid culture
  - Mice
- METHOD DETAILS
  - Organoid culture
  - Neuronal differentiation and culture
  - Cell culture
  - Plasmid construction
  - Lentivirus production and plasmid transduction
  - Library transduction and selection
  - Sample preparation for next-generation sequencing
  - CRISPR screen data analysis
  - Common essentials and GC-specific fitness genes
  - Analysis of Chronos data in organoid and GC cell lines
  - Target tractability
  - Pathway enrichment analysis
  - Flow cytometric analysis and cell sorting
  - Drug validation assay
  - Growth competition assay
  - DNA editing efficiency
  - GFP transfer assay
  - Immunocytochemistry
  - Western blot
  - Free fatty acid and triglyceride assays
  - Metabolomics analysis
  - Clinical data set
  - Gene knockout study in mice
  - Drug response study in mice
  - RNA-sequencing
  - Splicing analysis
- QUANTIFICATION AND STATISTICAL ANALYSIS

SUPPLEMENTAL INFORMATION

Supplemental information can be found online at https://doi.org/10.1016/j.stem.2025.08.006.

Received: January 24, 2025
Revised: June 30, 2025
Accepted: August 5, 2025
Published: September 2, 2025

REFERENCES

1. de Visser, K.E., and Joyce, J.A. (2023). The evolving tumor microenvironment: From cancer initiation to metastatic outgrowth. Cancer Cell *41*, 374–403. https://doi.org/10.1016/j.ccell.2023.02.016.
2. Zahalka, A.H., and Frenette, P.S. (2020). Nerves in cancer. Nat. Rev. Cancer *20*, 143–157. https://doi.org/10.1038/s41568-019-0237-2.
3. Vaes, N., Idris, M., Boesmans, W., Alves, M.M., and Melotte, V. (2022). Nerves in gastrointestinal cancer: from mechanism to modulations. Nat. Rev. Gastroenterol. Hepatol. *19*, 768–784. https://doi.org/10.1038/s41575-022-00669-9.
4. Clevers, H., and Tuveson, D.A. (2019). Organoid Models for Cancer Research. Annu. Rev. Cancer Biol. *3*, 223–234. https://doi.org/10.1146/annurev-cancerbio-030518-055702.
5. Polak, R., Zhang, E.T., and Kuo, C.J. (2024). Cancer organoids 2.0: modelling the complexity of the tumour immune microenvironment. Nat. Rev. Cancer *24*, 523–539. https://doi.org/10.1038/s41568-024-00706-6.
6. Behan, F.M., Iorio, F., Picco, G., Gonçalves, E., Beaver, C.M., Migliardi, G., Santos, R., Rao, Y., Sassi, F., Pinnelli, M., et al. (2019). Prioritization of cancer therapeutic targets using CRISPR-Cas9 screens. Nature *568*, 511–516. https://doi.org/10.1038/s41586-019-1103-9.
7. Pacini, C., Duncan, E., Gonçalves, E., Gilbert, J., Bhosle, S., Horswell, S., Karakoc, E., Lightfoot, H., Curry, E., Muyas, F., et al. (2024). A comprehensive clinically informed map of dependencies in cancer cells and framework for target prioritization. Cancer Cell *42*, 301–316.e9. https://doi.org/10.1016/j.ccell.2023.12.016.
8. Michels, B.E., Mosa, M.H., Streibl, B.I., Zhan, T., Menche, C., Abou-El-Ardat, K., Darvishi, T., Członka, E., Wagner, S., Winter, J., et al. (2020). Pooled In Vitro and In Vivo CRISPR-Cas9 Screening Identifies Tumor Suppressors in Human Colon Organoids. Cell Stem Cell *26*, 782–792.e7. https://doi.org/10.1016/j.stem.2020.04.003.
9. Ringel, T., Frey, N., Ringnalda, F., Janjuha, S., Cherkaoui, S., Butz, S., Srivatsa, S., Pirkl, M., Russo, G., Villiger, L., et al. (2020). Genome-Scale CRISPR Screening in Human Intestinal Organoids Identifies Drivers of TGF-beta Resistance. Cell Stem Cell *26*, 431–440.e8. https://doi.org/10.1016/j.stem.2020.02.007.
10. Murakami, K., Terakado, Y., Saito, K., Jomen, Y., Takeda, H., Oshima, M., and Barker, N. (2021). A genome-scale CRISPR screen reveals factors regulating Wnt-dependent renewal of mouse gastric epithelial cells. Proc. Natl. Acad. Sci. USA *118*, e2016806118. https://doi.org/10.1073/pnas.2016806118.
11. Ungricht, R., Guibbal, L., Lasbennes, M.C., Orsini, V., Beibel, M., Waldt, A., Cuttat, R., Carbone, W., Basler, A., Roma, G., et al. (2022). Genome-wide screening in human kidney organoids identifies developmental and disease-related aspects of nephrogenesis. Cell Stem Cell *29*, 160–175.e7. https://doi.org/10.1016/j.stem.2021.11.001.
12. Mircetic, J., Camgöz, A., Abohawya, M., Ding, L., Dietzel, J., Tobar, S.G., Paszkowski-Rogacz, M., Seidlitz, T., Schmäche, T., Mehnert, M.C., et al. (2023). CRISPR/Cas9 Screen in Gastric Cancer Patient-Derived Organoids Reveals KDM1A-NDRG1 Axis as a Targetable Vulnerability. Small Methods *7*, e2201605. https://doi.org/10.1002/smtd.202201605.
13. Hansen, S.L., Larsen, H.L., Pikkupeura, L.M., Maciag, G., Guiu, J., Müller, I., Clement, D.L., Mueller, C., Johansen, J.V., Helin, K., et al. (2023). An organoid-based CRISPR-Cas9 screen for regulators of

intestinal epithelial maturation and cell fate. Sci. Adv. *9*, eadg4055. https://doi.org/10.1126/sciadv.adg4055.

14. Andreatta, F., Hendriks, D., and Artegiani, B. (2025). Human Organoids as an Emerging Tool for Genome Screenings. Annu. Rev. Biomed. Eng. *27*, 157–183. https://doi.org/10.1146/annurev-bioeng-103023-122327.
15. Yan, H.H.N., Siu, H.C., Law, S., Ho, S.L., Yue, S.S.K., Tsui, W.Y., Chan, D., Chan, A.S., Ma, S., Lam, K.O., et al. (2018). A Comprehensive Human Gastric Cancer Organoid Biobank Captures Tumor Subtype Heterogeneity and Enables Therapeutic Screening. Cell Stem Cell *23*, 882–897.e11. https://doi.org/10.1016/j.stem.2018.09.016.
16. Tong, Y., Cheng, P.S.W., Or, C.S., Yue, S.S.K., Siu, H.C., Ho, S.L., Law, S.Y.K., Tsui, W.Y., Chan, D., Ma, S., et al. (2023). Escape from cell-cell and cell-matrix adhesion dependence underscores disease progression in gastric cancer organoid models. Gut *72*, 242–255. https://doi.org/10.1136/gutjnl-2022-327121.
17. Doench, J.G., Fusi, N., Sullender, M., Hegde, M., Vaimberg, E.W., Donovan, K.F., Smith, I., Tothova, Z., Wilen, C., Orchard, R., et al. (2016). Optimized sgRNA design to maximize activity and minimize off-target effects of CRISPR-Cas9. Nat. Biotechnol. *34*, 184–191. https://doi.org/10.1038/nbt.3437.
18. Li, W., Xu, H., Xiao, T., Cong, L., Love, M.I., Zhang, F., Irizarry, R.A., Liu, J.S., Brown, M., and Liu, X.S. (2014). MAGeCK enables robust identification of essential genes from genome-scale CRISPR/Cas9 knockout screens. Genome Biol. *15*, 554. https://doi.org/10.1186/s13059-014-0554-4.
19. Kim, E., and Hart, T. (2021). Improved analysis of CRISPR fitness screens and reduced off-target effects with the BAGEL2 gene essentiality classifier. Genome Med. *13*, 2. https://doi.org/10.1186/s13073-020-00809-3.
20. Hart, T., Brown, K.R., Sircoulomb, F., Rottapel, R., and Moffat, J. (2014). Measuring error rates in genomic perturbation screens: gold standards for human functional genomics. Mol. Syst. Biol. *10*, 733. https://doi.org/10.15252/msb.20145216.
21. Hart, T., Tong, A.H.Y., Chan, K., Van Leeuwen, J., Seetharaman, A., Aregger, M., Chandrashekhar, M., Hustedt, N., Seth, S., Noonan, A., et al. (2017). Evaluation and Design of Genome-Wide CRISPR/SpCas9 Knockout Screens. G3 (Bethesda) *7*, 2719–2727. https://doi.org/10.1534/g3.117.041277.
22. Dempster, J.M., Boyle, I., Vazquez, F., Root, D.E., Boehm, J.S., Hahn, W.C., Tsherniak, A., and McFarland, J.M. (2021). Chronos: a cell population dynamics model of CRISPR experiments that improves inference of gene fitness effects. Genome Biol. *22*, 343. https://doi.org/10.1186/s13059-021-02540-7.
23. Kuntz, E.M., Baquero, P., Michie, A.M., Dunn, K., Tardito, S., Holyoake, T.L., Helgason, G.V., and Gottlieb, E. (2017). Targeting mitochondrial oxidative phosphorylation eradicates therapy-resistant chronic myeloid leukemia stem cells. Nat. Med. *23*, 1234–1240. https://doi.org/10.1038/nm.4399.
24. Sancho, P., Barneda, D., and Heeschen, C. (2016). Hallmarks of cancer stem cell metabolism. Br. J. Cancer *114*, 1305–1312. https://doi.org/10.1038/bjc.2016.152.
25. Brown, K.K., Hann, M.M., Lakdawala, A.S., Santos, R., Thomas, P.J., and Todd, K. (2018). Approaches to target tractability assessment - a practical perspective. MedChemComm *9*, 606–613. https://doi.org/10.1039/c7md00633k.
26. Schneider, M., Radoux, C.J., Hercules, A., Ochoa, D., Dunham, I., Zalmas, L.P., Hessler, G., Ruf, S., Shanmugasundaram, V., Hann, M. M., et al. (2021). The PROTACtable genome. Nat. Rev. Drug Discov. *20*, 789–797. https://doi.org/10.1038/s41573-021-00245-x.
27. Singh, K.K., Wachsmuth, L., Kulozik, A.E., and Gehring, N.H. (2013). Two mammalian MAGOH genes contribute to exon junction complex composition and nonsense-mediated decay. RNA Biol. *10*, 1291–1298. https://doi.org/10.4161/rna.25827.
28. Barreiro, R.A.S., Guardia, G.D.A., Meliso, F.M., Lei, X., Li, W.Q., Savio, A., Fellermeyer, M., Conceição, H.B., Mercuri, R.L.V., Landry, T., et al. (2023). The paralogues MAGOH and MAGOHB are oncogenic factors in high-grade gliomas and safeguard the splicing of cell division and cell cycle genes. RNA Biol. *20*, 311–322. https://doi.org/10.1080/15476286.2023.2221511.
29. Molina, J.R., Sun, Y., Protopopova, M., Gera, S., Bandi, M., Bristow, C., McAfoos, T., Morlacchi, P., Ackroyd, J., Agip, A.A., et al. (2018). An inhibitor of oxidative phosphorylation exploits cancer vulnerability. Nat. Med. *24*, 1036–1046. https://doi.org/10.1038/s41591-018-0052-4.
30. Harriman, G., Greenwood, J., Bhat, S., Huang, X., Wang, R., Paul, D., Tong, L., Saha, A.K., Westlin, W.F., Kapeller, R., and Harwood, H.J., Jr. (2016). Acetyl-CoA carboxylase inhibition by ND-630 reduces hepatic steatosis, improves insulin sensitivity, and modulates dyslipidemia in rats. Proc. Natl. Acad. Sci. USA *113*, E1796–E1805. https://doi.org/10.1073/pnas.1520686113.
31. Svensson, R.U., Parker, S.J., Eichner, L.J., Kolar, M.J., Wallace, M., Brun, S.N., Lombardo, P.S., Van Nostrand, J.L., Hutchins, A., Vera, L., et al. (2016). Inhibition of acetyl-CoA carboxylase suppresses fatty acid synthesis and tumor growth of non-small-cell lung cancer in preclinical models. Nat. Med. *22*, 1108–1119. https://doi.org/10.1038/nm.4181.
32. Falchook, G., Infante, J., Arkenau, H.T., Patel, M.R., Dean, E., Borazanci, E., Brenner, A., Cook, N., Lopez, J., Pant, S., et al. (2021). First-in-human study of the safety, pharmacokinetics, and pharmacodynamics of first-in-class fatty acid synthase inhibitor TVB-2640 alone and with a taxane in advanced tumors. EClinicalmedicine *34*, 100797. https://doi.org/10.1016/j.eclinm.2021.100797.
33. Chang, L., Ruiz, P., Ito, T., and Sellers, W.R. (2021). Targeting pan-essential genes in cancer: Challenges and opportunities. Cancer Cell *39*, 466–479. https://doi.org/10.1016/j.ccell.2020.12.008.
34. Han, K., Pierce, S.E., Li, A., Spees, K., Anderson, G.R., Seoane, J.A., Lo, Y.H., Dubreuil, M., Olivas, M., Kamber, R.A., et al. (2020). CRISPR screens in cancer spheroids identify 3D growth-specific vulnerabilities. Nature *580*, 136–141. https://doi.org/10.1038/s41586-020-2099-x.
35. Kim, J., Koo, B.K., and Knoblich, J.A. (2020). Human organoids: model systems for human biology and medicine. Nat. Rev. Mol. Cell Biol. *21*, 571–584. https://doi.org/10.1038/s41580-020-0259-3.
36. Drost, J., and Clevers, H. (2018). Organoids in cancer research. Nat. Rev. Cancer *18*, 407–418. https://doi.org/10.1038/s41568-018-0007-6.
37. Else, P.L. (2020). The highly unnatural fatty acid profile of cells in culture. Prog. Lipid Res. *77*, 101017. https://doi.org/10.1016/j.plipres.2019.101017.
38. Saini, R.K., and Keum, Y.S. (2018). Omega-3 and omega-6 polyunsaturated fatty acids: Dietary sources, metabolism, and significance - A review. Life Sci. *203*, 255–267. https://doi.org/10.1016/j.lfs.2018.04.049.
39. Ackerman, D., Tumanov, S., Qiu, B., Michalopoulou, E., Spata, M., Azzam, A., Xie, H., Simon, M.C., and Kamphorst, J.J. (2018). Triglycerides Promote Lipid Homeostasis during Hypoxic Stress by Balancing Fatty Acid Saturation. Cell Rep. *24*, 2596–2605.e5. https://doi.org/10.1016/j.celrep.2018.08.015.
40. Wunderling, K., Zurkovic, J., Zink, F., Kuerschner, L., and Thiele, C. (2023). Triglyceride cycling enables modification of stored fatty acids. Nat. Metab. *5*, 699–709. https://doi.org/10.1038/s42255-023-00769-z.
41. Schledwitz, A., Xie, G., and Raufman, J.P. (2021). Exploiting unique features of the gut-brain interface to combat gastrointestinal cancer. J. Clin. Invest. *131*, e143776. https://doi.org/10.1172/JCI143776.
42. Duchalais, E., Guilluy, C., Nedellec, S., Touvron, M., Bessard, A., Touchefeu, Y., Bossard, C., Boudin, H., Louarn, G., Neunlist, M., and Van Landeghem, L. (2018). Colorectal Cancer Cells Adhere to and Migrate Along the Neurons of the Enteric Nervous System. Cell. Mol. Gastroenterol. Hepatol. *5*, 31–49. https://doi.org/10.1016/j.jcmgh.2017.10.002.
43. Tu, R.H., Wu, S.Z., Huang, Z.N., Zhong, Q., Ye, Y.H., Zheng, C.H., Xie, J.W., Wang, J.B., Lin, J.X., Chen, Q.Y., et al. (2023). Neurotransmitter Receptor HTR2B Regulates Lipid Metabolism to Inhibit Ferroptosis in Gastric Cancer. Cancer Res. *83*, 3868–3885. https://doi.org/10.1158/0008-5472.CAN-23-1012.

44. Rabben, H.L., Andersen, G.T., Olsen, M.K., Øverby, A., Ianevski, A., Kainov, D., Wang, T.C., Lundgren, S., Grønbech, J.E., Chen, D., and Zhao, C.M. (2021). Neural signaling modulates metabolism of gastric cancer. iScience *24*, 102091. https://doi.org/10.1016/j.isci.2021.102091.

45. Tang, R., Murray, C.W., Linde, I.L., Kramer, N.J., Lyu, Z., Tsai, M.K., Chen, L.C., Cai, H., Gitler, A.D., Engleman, E., et al. (2020). A versatile system to record cell-cell interactions. Elife *9*, e61080. https://doi.org/10.7554/eLife.61080.

46. Phillips, R.E., Yang, Y., Smith, R.C., Thompson, B.M., Yamasaki, T., Soto-Feliciano, Y.M., Funato, K., Liang, Y., Garcia-Bermudez, J., Wang, X., et al. (2019). Target identification reveals lanosterol synthase as a vulnerability in glioma. Proc. Natl. Acad. Sci. USA *116*, 7957–7962. https://doi.org/10.1073/pnas.1820989116.

47. Nguyen, T.P., Wang, W., Sternisha, A.C., Corley, C.D., Wang, H.L., Wang, X., Ortiz, F., Lim, S.K., Abdullah, K.G., Parada, L.F., et al. (2023). Selective and brain-penetrant lanosterol synthase inhibitors target glioma stem-like cells by inducing 24(S),25-epoxycholesterol production. Cell Chem. Biol. *30*, 214–229.e18. https://doi.org/10.1016/j.chembiol.2023.01.005.

48. Parisi, L.R., Li, N., and Atilla-Gokcumen, G.E. (2017). Very Long Chain Fatty Acids Are Functionally Involved in Necroptosis. Cell Chem. Biol. *24*, 1445–1454.e8. https://doi.org/10.1016/j.chembiol.2017.08.026.

49. Lu, D., Parisi, L.R., Gokcumen, O., and Atilla-Gokcumen, G.E. (2023). SREBP activation contributes to fatty acid accumulations in necroptosis. RSC Chem. Biol. *4*, 310–322. https://doi.org/10.1039/d2cb00172a.

50. Parisi, L.R., Sowlati-Hashjin, S., Berhane, I.A., Galster, S.L., Carter, K.A., Lovell, J.F., Chemler, S.R., Karttunen, M., and Atilla-Gokcumen, G.E. (2019). Membrane Disruption by Very Long Chain Fatty Acids during Necroptosis. ACS Chem. Biol. *14*, 2286–2294. https://doi.org/10.1021/acschembio.9b00616.

51. Griffith, D.A., Kung, D.W., Esler, W.P., Amor, P.A., Bagley, S.W., Beysen, C., Carvajal-Gonzalez, S., Doran, S.D., Limberakis, C., Mathiowetz, A.M., et al. (2014). Decreasing the rate of metabolic ketone reduction in the discovery of a clinical acetyl-CoA carboxylase inhibitor for the treatment of diabetes. J. Med. Chem. *57*, 10512–10526. https://doi.org/10.1021/jm5016022.

52. Calle, R.A., Amin, N.B., Carvajal-Gonzalez, S., Ross, T.T., Bergman, A., Aggarwal, S., Crowley, C., Rinaldi, A., Mancuso, J., Aggarwal, N., et al. (2021). ACC inhibitor alone or co-administered with a DGAT2 inhibitor in patients with non-alcoholic fatty liver disease: two parallel, placebo-controlled, randomized phase 2a trials. Nat. Med. *27*, 1836–1848. https://doi.org/10.1038/s41591-021-01489-1.

53. Huard, K., Smith, A.C., Cappon, G., Dow, R.L., Edmonds, D.J., El-Kattan, A., Esler, W.P., Fernando, D.P., Griffith, D.A., Kalgutkar, A.S., et al. (2020). Optimizing the Benefit/Risk of Acetyl-CoA Carboxylase Inhibitors through Liver Targeting. J. Med. Chem. *63*, 10879–10896. https://doi.org/10.1021/acs.jmedchem.0c00640.

54. Kelly, K.L., Reagan, W.J., Sonnenberg, G.E., Clasquin, M., Hales, K., Asano, S., Amor, P.A., Carvajal-Gonzalez, S., Shirai, N., Matthews, M.D., et al. (2020). De novo lipogenesis is essential for platelet production in humans. Nat. Metab. *2*, 1163–1178. https://doi.org/10.1038/s42255-020-00272-9.

55. Lally, J.S.V., Ghoshal, S., DePeralta, D.K., Moaven, O., Wei, L., Masia, R., Erstad, D.J., Fujiwara, N., Leong, V., Houde, V.P., et al. (2019). Inhibition of Acetyl-CoA Carboxylase by Phosphorylation or the Inhibitor ND-654 Suppresses Lipogenesis and Hepatocellular Carcinoma. Cell Metab. *29*, 174–182.e5. https://doi.org/10.1016/j.cmet.2018.08.020.

56. Oth, M., Franz, M., Timmermans, J., and Möes, A. (1992). The bilayer floating capsule: a stomach-directed drug delivery system for misoprostol. Pharm. Res. *9*, 298–302. https://doi.org/10.1023/a:1015870314340.

57. Morand, O.H., Aebi, J.D., Dehmlow, H., Ji, Y.H., Gains, N., Lengsfeld, H., and Himber, J. (1997). Ro 48-8.071, a new 2,3-oxidosqualene:lanosterol cyclase inhibitor lowering plasma cholesterol in hamsters, squirrel monkeys, and minipigs: comparison to simvastatin. J. Lipid Res. *38*, 373–390. https://doi.org/10.1016/S0022-2275(20)37449-6.

58. Nair, A.B., and Jacob, S. (2016). A simple practice guide for dose conversion between animals and human. J. Basic Clin. Pharm. *7*, 27–31. https://doi.org/10.4103/0976-0105.177703.

59. Zhao, Z., Chen, X., Dowbaj, A.M., Sljukic, A., Bratlie, K., Lin, L., Fong, E.L.S., Balachander, G.M., Chen, Z., Soragni, A., et al. (2022). Organoids. Nat. Rev. Methods Primers *2*, 94. https://doi.org/10.1038/s43586-022-00174-y.

60. Broadfield, L.A., Pane, A.A., Talebi, A., Swinnen, J.V., and Fendt, S.M. (2021). Lipid metabolism in cancer: New perspectives and emerging mechanisms. Dev. Cell *56*, 1363–1393. https://doi.org/10.1016/j.devcel.2021.04.013.

61. Shi, J., Lv, Q., Miao, D., Xiong, Z., Wei, Z., Wu, S., Tan, D., Wang, K., and Zhang, X. (2024). HIF2alpha Promotes Cancer Metastasis through TCF7L2-Dependent Fatty Acid Synthesis in ccRCC. Research (Wash D. C) *7*, 0322. https://doi.org/10.34133/research.0322.

62. Choudhry, H., and Harris, A.L. (2018). Advances in Hypoxia-Inducible Factor Biology. Cell Metab. *27*, 281–298. https://doi.org/10.1016/j.cmet.2017.10.005.

63. Hazlehurst, J.M., Lim, T.R., Charlton, C., Miller, J.J., Gathercole, L.L., Cornfield, T., Nikolaou, N., Harris, S.E., Moolla, A., Othonos, N., et al. (2022). Acute intermittent hypoxia drives hepatic de novo lipogenesis in humans and rodents. Metabol. Open *14*, 100177. https://doi.org/10.1016/j.metop.2022.100177.

64. Won, Y., Jang, B., Lee, S.H., Reyzer, M.L., Presentation, K.S., Kim, H., Caldwell, B., Zhang, C., Lee, H.S., Lee, C., et al. (2024). Oncogenic Fatty Acid Metabolism Rewires Energy Supply Chain in Gastric Carcinogenesis. Gastroenterology *166*, 772–786.e14. https://doi.org/10.1053/j.gastro.2024.01.027.

65. Liu, Y., Gilchrist, A.E., Johansson, P.K., Guan, Y., Deras, J.D., Liu, Y.C., Ceva, S., Huang, M.S., Navarro, R.S., Enejder, A., et al. (2025). Engineered Hydrogels for Organoid Models of Human Nonalcoholic Fatty Liver Disease. Adv. Sci. (Weinh) *12*, e17332. https://doi.org/10.1002/advs.202417332.

66. Boehm, J.S., Garnett, M.J., Adams, D.J., Francies, H.E., Golub, T.R., Hahn, W.C., Iorio, F., McFarland, J.M., Parts, L., and Vazquez, F. (2021). Cancer research needs a better map. Nature *589*, 514–516. https://doi.org/10.1038/d41586-021-00182-0.

67. Price, S., Bhosle, S., Gonçalves, E., Li, X., McClurg, D.P., Barthorpe, S., Beck, A., Hall, C., Lightfoot, H., Farrow, L., et al. (2022). A suspension technique for efficient large-scale cancer organoid culturing and perturbation screens. Sci. Rep. *12*, 5571. https://doi.org/10.1038/s41598-022-09508-y.

68. van de Wetering, M., Francies, H.E., Francis, J.M., Bounova, G., Iorio, F., Pronk, A., van Houdt, W., van Gorp, J., Taylor-Weiner, A., Kester, L., et al. (2015). Prospective derivation of a living organoid biobank of colorectal cancer patients. Cell *161*, 933–945. https://doi.org/10.1016/j.cell.2015.03.053.

69. Yan, H.H.N., Siu, H.C., Ho, S.L., Yue, S.S.K., Gao, Y., Tsui, W.Y., Chan, D., Chan, A.S., Wong, J.W.H., Man, A.H.Y., et al. (2020). Organoid cultures of early-onset colorectal cancers reveal distinct and rare genetic profiles. Gut *69*, 2165–2179. https://doi.org/10.1136/gutjnl-2019-320019.

70. Guillen, K.P., Fujita, M., Butterfield, A.J., Scherer, S.D., Bailey, M.H., Chu, Z., DeRose, Y.S., Zhao, L., Cortes-Sanchez, E., Yang, C.H., et al. (2022). A human breast cancer-derived xenograft and organoid platform for drug discovery and precision oncology. Nat. Cancer *3*, 232–250. https://doi.org/10.1038/s43018-022-00337-6.

71. Sachs, N., de Ligt, J., Kopper, O., Gogola, E., Bounova, G., Weeber, F., Balgobind, A.V., Wind, K., Gracanin, A., Begthel, H., et al. (2018). A Living Biobank of Breast Cancer Organoids Captures Disease Heterogeneity. Cell *172*, 373–386.e10. https://doi.org/10.1016/j.cell.2017.11.010.

72. Gonçalves, E., Thomas, M., Behan, F.M., Picco, G., Pacini, C., Allen, F., Vinceti, A., Sharma, M., Jackson, D.A., Price, S., et al. (2021). Minimal genome-wide human CRISPR-Cas9 library. Genome Biol. *22*, 40. https://doi.org/10.1186/s13059-021-02268-4.

73. Geurts, M.H., and Clevers, H. (2023). CRISPR engineering in organoids for gene repair and disease modelling. Nat. Rev. Bioeng. *1*, 32–45. https://doi.org/10.1038/s44222-022-00013-5.

74. Wong, A.S.L., Choi, G.C.G., Cui, C.H., Pregernig, G., Milani, P., Adam, M., Perli, S.D., Kazer, S.W., Gaillard, A., Hermann, M., et al. (2016). Multiplexed barcoded CRISPR-Cas9 screening enabled by CombiGEM. Proc. Natl. Acad. Sci. USA *113*, 2544–2549. https://doi.org/10.1073/pnas.1517883113.

75. Zhou, P., Chan, B.K.C., Wan, Y.K., Yuen, C.T.L., Choi, G.C.G., Li, X., Tong, C.S.W., Zhong, S.S.W., Sun, J., Bao, Y., et al. (2020). A Three-Way Combinatorial CRISPR Screen for Analyzing Interactions among Druggable Targets. Cell Rep. *32*, 108020. https://doi.org/10.1016/j.celrep.2020.108020.

76. Han, K., Jeng, E.E., Hess, G.T., Morgens, D.W., Li, A., and Bassik, M.C. (2017). Synergistic drug combinations for cancer identified in a CRISPR screen for pairwise genetic interactions. Nat. Biotechnol. *35*, 463–474. https://doi.org/10.1038/nbt.3834.

77. Xu, F., Tong, M., Tong, C.S.W., Chan, B.K.C., Chu, H.Y., Wong, T.L., Fong, J.H.C., Cheung, M.S.H., Mak, K.H.M., Pardeshi, L., et al. (2021). A Combinatorial CRISPR-Cas9 Screen Identifies Ifenprodil as an Adjunct to Sorafenib for Liver Cancer Treatment. Cancer Res. *81*, 6219–6232. https://doi.org/10.1158/0008-5472.CAN-21-1017.

78. Hoover, G., Gilbert, S., Curley, O., Obellianne, C., Lin, M.T., Hixson, W., Pierce, T.W., Andrews, J.F., Alexeyev, M.F., Ding, Y., et al. (2025). Nerve-to-cancer transfer of mitochondria during cancer metastasis. Nature *644*, 252–262. https://doi.org/10.1038/s41586-025-09176-8.

79. Hart, T., and Moffat, J. (2016). BAGEL: a computational framework for identifying essential genes from pooled library screens. BMC Bioinform. *17*, 164. https://doi.org/10.1186/s12859-016-1015-8.

80. Iorio, F., Behan, F.M., Gonçalves, E., Bhosle, S.G., Chen, E., Shepherd, R., Beaver, C., Ansari, R., Pooley, R., Wilkinson, P., et al. (2018). Unsupervised correction of gene-independent cell responses to CRISPR-Cas9 targeting. BMC Genomics *19*, 604. https://doi.org/10.1186/s12864-018-4989-y.

81. Vinceti, A., Karakoc, E., Pacini, C., Perron, U., De Lucia, R.R., Garnett, M.J., and Iorio, F. (2021). CoRe: a robustly benchmarked R package for identifying core-fitness genes in genome-wide pooled CRISPR-Cas9 screens. BMC Genomics *22*, 828. https://doi.org/10.1186/s12864-021-08129-5.

82. Allen, F., Behan, F., Khodak, A., Iorio, F., Yusa, K., Garnett, M., and Parts, L. (2019). JACKS: joint analysis of CRISPR/Cas9 knockout screens. Genome Res. *29*, 464–471. https://doi.org/10.1101/gr.238923.118.

83. Colic, M., Wang, G., Zimmermann, M., Mascall, K., McLaughlin, M., Bertolet, L., Lenoir, W.F., Moffat, J., Angers, S., Durocher, D., and Hart, T. (2019). Identifying chemogenetic interactions from CRISPR screens with drugZ. Genome Med. *11*, 52. https://doi.org/10.1186/s13073-019-0665-3.

84. Leek, J.T., Johnson, W.E., Parker, H.S., Jaffe, A.E., and Storey, J.D. (2012). The sva package for removing batch effects and other unwanted variation in high-throughput experiments. Bioinform. *28*, 882–883. https://doi.org/10.1093/bioinformatics/bts034.

85. Ge, S.X., Jung, D., and Yao, R. (2020). ShinyGO: a graphical gene-set enrichment tool for animals and plants. Bioinform. *36*, 2628–2629. https://doi.org/10.1093/bioinformatics/btz931.

86. Liao, Y., Smyth, G.K., and Shi, W. (2019). The R package Rsubread is easier, faster, cheaper and better for alignment and quantification of RNA sequencing reads. Nucleic Acids Res. *47*, e47. https://doi.org/10.1093/nar/gkz114.

87. Robinson, M.D., McCarthy, D.J., and Smyth, G.K. (2010). edgeR: a Bioconductor package for differential expression analysis of digital gene expression data. Bioinform. *26*, 139–140. https://doi.org/10.1093/bioinformatics/btp616.

88. Ritchie, M.E., Phipson, B., Wu, D., Hu, Y., Law, C.W., Shi, W., and Smyth, G.K. (2015). limma powers differential expression analyses for RNA-sequencing and microarray studies. Nucleic Acids Res. *43*, e47. https://doi.org/10.1093/nar/gkv007.

89. Dobin, A., Davis, C.A., Schlesinger, F., Drenkow, J., Zaleski, C., Jha, S., Batut, P., Chaisson, M., and Gingeras, T.R. (2013). STAR: ultrafast universal RNA-seq aligner. Bioinform. *29*, 15–21. https://doi.org/10.1093/bioinformatics/bts635.

90. Haas, B.J., Dobin, A., Li, B., Stransky, N., Pochet, N., and Regev, A. (2019). Accuracy assessment of fusion transcript detection via read-mapping and de novo fusion transcript assembly-based methods. Genome Biol. *20*, 213. https://doi.org/10.1186/s13059-019-1842-9.

91. Shen, S., Park, J.W., Lu, Z.X., Lin, L., Henry, M.D., Wu, Y.N., Zhou, Q., and Xing, Y. (2014). rMATS: robust and flexible detection of differential alternative splicing from replicate RNA-Seq data. Proc. Natl. Acad. Sci. USA *111*, E5593–E5601. https://doi.org/10.1073/pnas.1419161111.

92. Schneider, C.A., Rasband, W.S., and Eliceiri, K.W. (2012). NIH Image to ImageJ: 25 years of image analysis. Nat. Methods *9*, 671–675. https://doi.org/10.1038/nmeth.2089.

93. Choi, G.C.G., Zhou, P., Yuen, C.T.L., Chan, B.K.C., Xu, F., Bao, S., Chu, H.Y., Thean, D., Tan, K., Wong, K.H., et al. (2019). Combinatorial mutagenesis en masse optimizes the genome editing activities of SpCas9. Nat. Methods *16*, 722–730. https://doi.org/10.1038/s41592-019-0473-0.

94. Aguirre, A.J., Meyers, R.M., Weir, B.A., Vazquez, F., Zhang, C.Z., Ben-David, U., Cook, A., Ha, G., Harrington, W.F., Doshi, M.B., et al. (2016). Genomic Copy Number Dictates a Gene-Independent Cell Response to CRISPR/Cas9 Targeting. Cancer Discov. *6*, 914–929. https://doi.org/10.1158/2159-8290.CD-16-0154.

95. Doench, J.G. (2018). Am I ready for CRISPR? A user's guide to genetic screens. Nat. Rev. Genet. *19*, 67–80. https://doi.org/10.1038/nrg.2017.97.

96. Vis, D.J., Bombardelli, L., Lightfoot, H., Iorio, F., Garnett, M.J., and Wessels, L.F. (2016). Multilevel models improve precision and speed of IC50 estimates. Pharmacogenomics *17*, 691–700. https://doi.org/10.2217/pgs.16.15.

97. Francies, H.E., Barthorpe, A., McLaren-Douglas, A., Barendt, W.J., and Garnett, M.J. (2019). Drug Sensitivity Assays of Human Cancer Organoid Cultures. Methods Mol. Biol. *1576*, 339–351. https://doi.org/10.1007/7651_2016_10.

98. Garnett, M.J., Edelman, E.J., Heidorn, S.J., Greenman, C.D., Dastur, A., Lau, K.W., Greninger, P., Thompson, I.R., Luo, X., Soares, J., et al. (2012). Systematic identification of genomic markers of drug sensitivity in cancer cells. Nature *483*, 570–575. https://doi.org/10.1038/nature11005.

99. Yu, H., Qu, T., Yang, J., and Dai, Q. (2023). Serotonin acts through YAP to promote cell proliferation: mechanism and implication in colorectal cancer progression. Cell Commun. Signal. *21*, 75. https://doi.org/10.1186/s12964-023-01096-2.

100. Maemura, K., Shiraishi, N., Sakagami, K., Kawakami, K., Inoue, T., Murano, M., Watanabe, M., and Otsuki, Y. (2009). Proliferative effects of gamma-aminobutyric acid on the gastric cancer cell line are associated with extracellular signal-regulated kinase 1/2 activation. J. Gastroenterol. Hepatol. *24*, 688–696. https://doi.org/10.1111/j.1440-1746.2008.05687.x.

101. Sarkar, C., Chakroborty, D., Chowdhury, U.R., Dasgupta, P.S., and Basu, S. (2008). Dopamine increases the efficacy of anticancer drugs in breast and colon cancer preclinical models. Clin. Cancer Res. *14*, 2502–2510. https://doi.org/10.1158/1078-0432.CCR-07-1778.

102. Tang, B., Wu, J., Zhu, M.X., Sun, X., Liu, J., Xie, R., Dong, T.X., Xiao, Y., Carethers, J.M., Yang, S., and Dong, H. (2019). VPAC1 couples with TRPV4 channel to promote calcium-dependent gastric cancer progression via a novel autocrine mechanism. Oncogene *38*, 3946–3961. https://doi.org/10.1038/s41388-019-0709-6.

103. Chakroborty, D., Goswami, S., Fan, H., Frankel, W.L., Basu, S., and Sarkar, C. (2022). Neuropeptide Y, a paracrine factor secreted by cancer cells, is an independent regulator of angiogenesis in colon cancer. Br. J. Cancer *127*, 1440–1449. https://doi.org/10.1038/s41416-022-01916-1.

104. Padmanaban, V., Keller, I., Seltzer, E.S., Ostendorf, B.N., Kerner, Z., and Tavazoie, S.F. (2024). Neuronal substance P drives metastasis through an extracellular RNA-TLR7 axis. Nature *633*, 207–215. https://doi.org/10.1038/s41586-024-07767-5.

105. O'Hara, A.M., Bhattacharyya, A., Bai, J., Mifflin, R.C., Ernst, P.B., Mitra, S., and Crowe, S.E. (2009). Tumor necrosis factor (TNF)-alpha-induced IL-8 expression in gastric epithelial cells: role of reactive oxygen species and AP endonuclease-1/redox factor (Ref)-1. Cytokine *46*, 359–369. https://doi.org/10.1016/j.cyto.2009.03.010.

106. Conant, D., Hsiau, T., Rossi, N., Oki, J., Maures, T., Waite, K., Yang, J., Joshi, S., Kelso, R., Holden, K., et al. (2022). Inference of CRISPR Edits from Sanger Trace Data. CRISPR J. *5*, 123–130. https://doi.org/10.1089/crispr.2021.0113.

107. Del Monte, U. (2009). Does the cell number 10(9) still really fit one gram of tumor tissue? Cell Cycle *8*, 505–506. https://doi.org/10.4161/cc.8.3.7608.

108. Liang, Y., Nephew, K.P., and Hyder, S.M. (2023). Cholesterol Biosynthesis Inhibitor RO 48-8071 Suppresses Growth of Epithelial Ovarian Cancer Cells in Vitro and In Vivo. J. Cancer Sci. Clin. Ther. *7*, 1–8. https://doi.org/10.26502/jcsct.5079185.

STAR★METHODS

KEY RESOURCES TABLE

REAGENT or RESOURCE	SOURCE	IDENTIFIER
Antibodies		
Rabbit anti-ACC1	Cell Signaling	Cat#4190S; RRID: AB_10547752
Rabbit anti-SREBP1	Abcam	Cat#ab28481; RRID: AB_778069
Rabbit anti-MLKL	Abcam	Cat#184718; RRID: AB_2755030
Rabbit anti-MLKL (phospho S358)	Abcam	Cat#187091; RRID: AB_2619685
Rabbit anti-ARHGAP26	Atlas Antibodies	Cat#HPA035107; RRID: AB_10669855
Mouse anti-neuron-specific beta-III tubulin	R&D systems	Cat#MAB1195; RRID: AB_357520
Rabbit anti-TrkC (C44H5)	Cell Signaling	Cat#3376; RRID: AB_2155283
Rabbit anti-MAP2	Cell Signaling	Cat#4542; RRID: AB_10693782
Rabbit GAPDH (14C10)	Cell Signaling	Cat#2118; RRID:AB_561053
PE/Cyanine7 anti-human CD49d antibody	BioLegend	Cat#304313; RRID: AB_10642817
Anti-rabbit IgG, HRP-linked antibody	Cell Signaling	Cat#7074; RRID: AB_2099233
Goat anti-Mouse IgG (H+L) Cross-absorbed secondary antibody, Alexa Fluor™ 488	ThermoFisher	Cat#A-11001; RRID: AB_2534069
Goat anti-Rabbit IgG (H+L)Cross-absorbed secondary antibody, Alexa Fluor™ 568	ThermoFisher	Cat#A-11011; RRID: AB_143157
ProLong™ Gold Antifade Mountant with DNA stain DAPI	Invitrogen	Cat#P36941; RRID: AB_2629482
Chemicals, peptides, and recombinant proteins		
Advanced DMEM/F12	Gibco	Cat#12634010
RPMI 1640	Gibco	Cat#11875093
DMEM	Gibco	Cat#10569010
Trypsin-EDTA	Gibco	Cat#25200072
HEPES	Gibco	Cat#15630080
GlutaMAX	Gibco	Cat#35050061
Penicillin-Streptomycin	Gibco	Cat#15140122
B-27 Supplement	Gibco	Cat#17504001
N-Acetyl-L-cysteine	Sigma-Aldrich	Cat#A9165
[Leu15]-Gastrin I human	Sigma-Aldrich	Cat#G9145
Recombinant Human EGF	Gibco	Cat#PHG0313
Recombinant Human FGF10	PeproTech	Cat#100-26
Recombinant Human R-Spondin-1	PeproTech	Cat#120-38
Recombinant Human Noggin	PeproTech	Cat#120-10C
WNT Surrogate-Fc Fusion Protein	IpA	Cat#N001
A83-01	Tocris	Cat#2939/10
Y-27632	Tocris	Cat#1254/10
Cultrex Reduced Growth Factor Basement Membrane Extract, Type 2 (BME)	R&D systems	Cat#3533-005-02
TrypLE™ Select	Gibco	Cat#12563029
Matrigel	Corning	Cat#354277
mTESR1	StemCell Technologies	Cat#85857
ReLeSR	StemCell Technologies	Cat#100-0484
Neurobasal medium	Gibco	Cat#21103049
BMP4	R&D systems	Cat#314-BP-010
SB431542	R&D systems	Cat#1614/10
CHIR99021	Tocris	Cat#4423
Retinoic acid	Tocris	Cat#0695

(*Continued on next page*)

Continued

REAGENT or RESOURCE	SOURCE	IDENTIFIER
DMH-1	Tocris	Cat#4126
Essential 6 medium	Gibco	Cat#A1516401
CTS™ N-2 supplement	Gibco	Cat#A1370701
MEM Non-essential amino acids solution	Gibco	Cat#11140050
Recombinant human GDNF	Peprotech	Cat#450-10
FGF2	Stemgent	Cat#03-0002
Accutase	Life Technologies	Cat#A11105-01
Poly-L-ornithine	Merck	Cat#P4957
Geltrex LDEV-Free, hESC-Qualified, reduced growth factor basement membrane matrix	Gibco	Cat#A1413302
Zeocin™	Invitrogen	Cat#R25001
Puromycin	InvivoGen	Cat#ant-pr-1
Ampicillin	Gold Biotechnology	Cat#A30125
Opti-MEM™	Gibco	Cat#31985070
PEI transfection reagent	MedChemExpress	Cat#HY-K2014
Dimethyl sulfoxide	Sigma-Aldrich	Cat#D2650
5-Fluorouracil	Sigma-Aldrich	Cat#F6627
IACS-010759	Cayman	Cat#25867
IM-156	Cayman	Cat#34763
ND630	Cayman	Cat#23961
ND646	Cayman	Cat#34764
Ro 48-8071 fumarate	MedChemExpress	Cat#HY-18630A
MG-132	Sigma-Aldrich	Cat#474790
Rotenone	Cayman	Cat#13995
TVB-2640	Cayman	Cat#35703
BSA Control for BSA-Fatty Acid Complexes	Cayman	Cat#29556
BSA-Palmitate Saturated Fatty Acid Complex	Cayman	Cat#29558
BSA-Oleate Monounsaturated Fatty Acid Complex	Cayman	Cat#29557
Acetylcholine	Merck	Cat#A2661
Acetate	Millipore	Cat#567422
Serotonin hydrochloride	MedChemExpress	Cat#HY-B1473
GABA	MedChemExpress	Cat#HY-N0067
Dopamine hydrochloride	MedChemExpress	Cat#HY-B0451A
VIP	MedChemExpress	Cat#HY-P1023
Neuropeptide Y	MedChemExpress	Cat#HY-P1601
Substance P	MedChemExpress	Cat#HY-P0201
TNF-α	MedChemExpress	Cat#HY-P1860
QuickExtract™ DNA Extraction Solution	Biosearch Technologies	Cat#QE09050
D-Luciferin, Potassium Salt	Gold Biotechnology	Cat#LUCK-1G
Tween 80	Sigma-Aldrich	Cat#P1754
PEG 400	Polysciences	Cat#25322-68-3
Pierce ECL Western Blotting Substrate	Thermo Scientific	Cat#32106
Critical commercial assays		
MiniBEST Plasmid Purification Kit	TaKaRa	Cat#9760
Plasmid Midi Kit	QIAGEN	Cat#12145
DNeasy Blood & Tissue Kit	QIAGEN	Cat#69506
MiniBEST Universal RNA Extraction Kit	TaKaRa	Cat#9767
Agencourt AMPure XP beads	Beckman Coulter	Cat#A63881
Cell titer-Glo® Luminescent Cell Viability Assay	Promega	Cat#G7572
Kapa HiFi HotStart ReadyMix	Kapa Biosystems	Cat#KK2602

(*Continued on next page*)

Continued

REAGENT or RESOURCE	SOURCE	IDENTIFIER
KAPA mRNA HyperPrep Kit	Kapa Biosystems	Cat#KK8580
SYBR® Premix Ex Taq™	TaKaRa	Cat#RR420
Free Fatty Acid Quantification Assay Kit	Abcam	Cat#ab65341
Triglyceride Quantification Assay Kit	Abcam	Cat# ab65336
Deposited data		
RNA-seq data	This study	GEO:GSE303453
Data S1	This study	Mendeley: https://doi.org/10.17632/8xh8sx232r.1
Experimental models: Cell lines		
HEK293T	ATCC	Cat#CRL-3216
Gastric cancer cell lines	Suet Yi Leung Laboratory	N/A
Patient-derived GC organoid lines	Yan et al.[15] and Tong et al,[16]	N/A
H9 hESC	Kathryn Song Eng Cheah Laboratory	N/A
Experimental models: Organisms/strains		
BALB/cAnN-nu mice	Charles River Laborattory	N/A
NOD/SCID mice	Charles River Laborattory	N/A
Oligonucleotides		
See Methods S1 for sgRNA sequences	This study	N/A
See Methods S1 for qRT-PCR primers	This study	N/A
Recombinant DNA		
See Methods S1 for plasmid constructs	This study	N/A
Software and algorithms		
RStudio v4.3.2	RStudio	https://www.r-project.org/
MAGeCK v0.5.9	Li et al.[18]	https://sourceforge.net/p/mageck/wiki/Home/
BAGEL	Hart et al.[79]	https://github.com/hart-lab/bagel
CRISPRcleanR	Iorio et al.[80]	https://github.com/francescojm/CRISPRcleanR
CoRe	Vinceti et al.[81]	https://github.com/DepMap-Analytics/CoRe/tree/master
Chronos	Dempster et al.[22]	https://github.com/broadinstitute/chronos
JACKS	Allen et al.[82]	https://github.com/felicityallen/JACKS
DrugZ	Colic et al[83]	https://github.com/hart-lab/drugz
sva v3.34.0	Leek et al.[84]	https://bioconductor.org/packages/release/bioc/html/sva.html
ShinyGO 0.76	Ge et al.[85]	http://bioinformatics.sdstate.edu/go76/
GSEA	Broad Institute	https://www.gsea-msigdb.org/gsea/msigdb/index.jsp
Rsubread	Liao et al.[86]	https://bioconductor.org/packages/release/bioc/html/Rsubread.html
edgeR	Robinson et al.[87]	https://bioconductor.org/packages/release/bioc/html/edgeR.html
limma	Ritchie et al.[88]	https://bioconductor.org/packages/release/bioc/html/limma.html
STAR v2.7.11b	Dobin et al.[89]	https://github.com/alexdobin/STAR/tree/master
STAR-Fusion v1.7.0	Hass et al.[90]	https://github.com/STAR-Fusion/STAR-Fusion/wiki
CTAT-splicing v0.0.3	National Cancer Institute	https://github.com/TrinityCTAT/CTAT-SPLICING/wiki
rMATS v4.1.1	Shen et al.[91]	https://github.com/Xinglab/rmats-turbo
Image J	Schneider et al.[92]	https://imagej.net/ij/
FlowJo v10.8.1	BD Biosciences	https://www.flowjo.com/
SPSS v25	IBM	https://www.ibm.com/products/spss
GraphPad Prism 9	GraphPad	https://www.graphpad.com/

EXPERIMENTAL MODEL AND SUBJECT DETAILS

Human material for organoid culture

Patient-derived organoids were obtained from the laboratory of Suet Yi Leung at the University of Hong Kong. Informed consent was obtained from all participants, and the study was approved by the Institutional Review Board of the University of Hong Kong and the Hospital Authority Hong Kong West Cluster (IRB reference ID: UW14-257).

Mice

All animal experimental procedures were approved by and performed in accordance with the Committee of the Use of Live Animals in Teaching and Research (CULATR) at The University of Hong Kong and the Animals (Control of Experiments) Ordinance of Hong Kong. The experiments conducted all complied with ethical regulations. 6- to 8-week-old male BALB/cAnN-nu mouse and NOD/SCID mouse were obtained from Charles River Laboratory and used for transplantation studies without any other interventions. Mice were housed in a pathogen-free animal facility in cages with up to five animals at the Centre for Comparative Medicine Research at The University of Hong Kong and kept in a temperature- and humidity-controlled room on a 12-h light-dark cycle.

METHOD DETAILS

Organoid culture

Establishment and maintenance of GC organoid cultures were performed as previously described[15] with slight modifications. In brief, organoids were dissociated mechanically by pipetting after incubating in TrypLE (Gibco) at 37°C for 5-10 minutes. This procedure was repeated once or twice, depending on the size and tightness of the organoids. Organoids were then washed with advanced DMEM/F12 containing 1x P/S, 1x GlutaMAX, and 1x HEPES (Ad+++) (Gibco) and subsequently embedded in 80% basement membrane extract (BME; R&D systems) diluted with complete medium supplemented with 250 μM Wnt surrogate (IpA), 500 ng/ml RSPO-1(PeproTech), 100 ng/ml Noggin (PeproTech), 1x B27 (Gibco), 50 ng/ml EGF (Gibco), 100 ng/ml FGF10 (PeproTech), 1 mM NAC (Sigma-Aldrich), 1 nM Gastrin (Sigma-Aldrich) and 2 μM A83-01 (Tocris). Upon seeding of BME domes, 2 ml complete medium supplemented with 10 μM Y-27632 (Tocris) was added after passage, and culture medium was changed every 2-3 days. Culture procedures were consistent across organoid lines with varying passage numbers, and the stability of GC organoids was maintained, even during long-term culture.[15] All stable Cas9-expressing GC organoids tested exhibited a similar degree of knockout activity mediated by Cas9 and achieved a high indel percentage at the selected endogenous target loci (Figures S2B and S2C).

Neuronal differentiation and culture

H9 hESC was cultured in mTESR1 on Matrigel (Corning) and was expanded for neural crest differentiation. Confluent hESCs were washed with phosphate-buffered saline (PBS), followed by a detachment of undifferentiated cells with ReLeSR (StemCell Technologies). Thereafter, cell aggregates were replated on Matrigel and fed with a medium consisting of 20 ng/ml BMP4 (R&D systems), 2 μM SB431542 (R&D systems), 1 μM CHIR99021 (Tocris), 1uM retinoic acid (Tocris), and 1 μM DMH-1 (Tocris) in Essential 6 medium (Thermo Fisher). Differentiated enteric neural crest cell (ENCC) populations were purified by FACS using CD49C surface marker staining (BioLegend). The purified ENCCs were cultured as free-floating 3D spheroids in an ultra-low binding plate (Corning) and maintained in neural crest culture medium (NCCM) consisting of 1% N2 (Gibco), 2% B27 (Gibco), 1% MEM non-essential amino acid (Gibco), 1% GlutaMAX (Gibco), 3 μM CHIR99021 (Tocris), and 10 ng/ml FGF2 (Stemgent) in neurobasal medium (Gibco). 10 μM Y-27632 (Tocris) was added after passage, and the culture medium was changed every 2 days. For enteric neuron differentiation, ENCCs were dissociated with Accutase (Life Technologies) into single cells and plated on a culture dish coated with poly-L-ornithine (Merck) and reduced growth factor basement membrane matrix (Gibco). Cells were fed with NCCM without FGF2 and CHIR99012 and supplemented with 10 ng/ml GDNF (PeproTech). After 30-40 days of differentiation, differentiated ENs were analyzed by detecting the expressions of differentiation and neural markers by qPCR and immunocytochemistry. ENs exhibited elevated levels of *DCX*, *NeuN*, and *TUBB3* expressions, indicating the presence of both immature and mature neurons in the Day 40 culture. This confirms the transition from neural progenitor cells to neuronal cells. The increased expression of MAP2 and SYP suggests the development of neurite branching and functional synapses. High levels of EN-derived progenitor markers such as *GFRA1*, *ASCL1*, and *PHOX2B* indicate the presence of early enteric neurons. Notably, elevated *EDNRB* expression was observed in EN. *EDNRB* is involved in the proliferation of uncommitted EN progenitor cells, and its expression should have decreased during ENC induction. Nevertheless, the upregulation of *SST*, *CHAT*, *TH*, and *HTR2A* gene expressions indicated the progression of neuronal commitment and maturity throughout the differentiation process.

Cell culture

SNU-1, HGC-27, AGS, MKN-45, KATO III, NUGC-3, and SNU-16 were maintained in RPMI 1640 medium. HEK293T cells were maintained in DMEM. SNU-1-Cas9, HGC-27-Cas9, AGS-Cas9, and MKN-45-Cas9 cells were generated by transducing pAWp63-clone32 (Addgene, 131736)[93] into the parental cells, followed by 1-2 weeks of zeocin (200 - 400 μg/ml) selection. All cells were grown in culture medium (RPMI 1640 or DMEM, 10% fetal bovine serum (FBS), 1% antibiotic-antimycotic) at 37°C with 5% CO_2. To aid the formation of 3D spheroids and organoid-like structures, we cultured 2D cell lines using two methods, i.e., ultra-low binding plates or BME coating, respectively. Cells were seeded into a 96-well ultra-low binding plate at ~10% cell confluency with culture medium. For

BME coating, the same number of cells were seeded in a regular 96-well culture plate coated with a thick layer of BME (50 μl; 50% BME mixed with 50% culture medium) and fed with 100 μl culture medium.

Plasmid construction

The plasmids used in this study (Methods S1) were purchased from Addgene or generated by standard molecular cloning strategies, including PCR, oligo annealing, restriction enzyme digestion, and ligation. Custom oligonucleotides were purchased from Genewiz. Oligo pairs with the selected sgRNA target sequences (Methods S1) were annealed and cloned into the Esp3I-digested KMp56 lentiviral vector. Ligated vectors were transformed into *E. coli* strain DH5α competent cells and selected with ampicillin (100 μg/ml). DNA was extracted and purified by Plasmid Mini (TaKaRa) or Midi (QIAGEN) preparation kits. Sequences of vectors were verified by Sanger sequencing.

Lentivirus production and plasmid transduction

Lentivirus was produced by transfecting HEK293T cells of ∼70% confluency in a 15-cm dish with 9 μg of pCMV-VSV-G vector (Addgene, 8454), 18 μg of pCMV-dR8.2-dvpr (Addgene, 8455) vector and 9 μg of the respective lentiviral vector mixed with 1.8 ml Opti-MEM (Gibco) and 90 μl PEI (2 mg/ml) (MedChemExpress). The mixture was vortexed briefly and incubated at room temperature for 20 minutes prior to transduction. The culture medium was replaced with a fresh culture medium the next day. Viral supernatants were collected at 48 and 72 hr post-transfection. Two batches of viral media were combined, filtered by 0.45 μm polyethersulfone membrane (Pall), and concentrated 100X by centrifugation at 4,000 g for 2 hr with Amicon® Ultra centrifugal filter unit (Millipore). 2 μl of the concentrated virus medium was added into one well of a 12-well plate with ∼30% cell confluency for routine cell line transduction, whereas approximately 5- to 10-fold more virus medium was required to obtain a comparable infection rate in a similar condition in organoids.

Library transduction and selection

For the genome-wide CRISPR screen, we chose an organoid (GX117-T1O) that has a fast-growing rate (with a doubling time of ∼32.5 hours) that allows us to quickly generate enough organoids for the large-scale CRISPR screen (Table S2). This organoid was derived from a genomically stable tumor to minimize false positives resulting from gene-independent anti-proliferative cell responses, especially in copy number amplified regions.[94] Organoids were dissociated into single cells and transduced with the lentiviral Brunello genome-wide library (Addgene, 73178) at a multiplicity of infection (MOI) of ∼0.3 for 12-16 hr. This library was chosen based on their previously reported high Rule Set 2 scores (which maximized on-target activity) and high CFD scores (which minimized off-target sites).[17] The low MOI was used to ensure most of the infected cells contained only one sgRNA. Infected organoids were then selected by puromycin (2 μg/ml) for 4 days. Patient-derived organoids resemble the *in vivo* tumors, which can be heterogeneous in nature. CRISPR screening in organoids could identify genetic dependencies that, when being targeted, are the most effective in suppressing the growth of the heterogeneous pool of tumor cells in patients. To account for the heterogenicity among the organoid cells and compensate for the stochastic loss of sgRNA in the CRISPR dropout screen, we transduced the Cas9-expressing organoids with the sgRNA library to obtain large organoid pools with a 200-fold representation of the library size after puromycin selection. Thus, to maintain at least a 200-fold representation of the infected cells after selection, 5×10^7 single cells per replicate (∼650-fold) were used at the start of the experiment. We obtained a high library coverage and a uniform distribution of the sgRNAs within the plasmid and infected organoid pools (Figure S1A). Infected cells embedded in BME were cultured and expanded until day 21 post-infection (∼15 rounds of cell doubling) for dropout to occur, and the screen was performed in two biological replicates (Figure S1B). For the CRISPR screen with a focused library derived from gene hits identified in the genome-wide organoid screen, 6×10^6 single cells were transduced with the lentiviral library containing 1,436 sgRNAs that target the 303 genes, 28 essential genes, and 28 non-essential genes at a MOI of ∼0.3 for 12-16 hrs. On day 7 post-infection, successfully transduced cells indicated by EGFP signal were sorted out, cultured, and expanded until day 21 post-infection to ensure 400-fold coverage at genomic DNA collection. *In vivo* CRISPR dropout screens are subject to greater variations than *in vitro* screens because of the uncertain number of cells that would be successfully engrafted and contribute to the *in vivo* tumor,[95] but offer the advantage of reducing animal experimentation for gene-by-gene testing. For our *in vivo* CRISPR dropout assay, we limited our selection to five genes and aimed for a larger library representation to lessen the variations. 12 plasmids, of which 10 contained sgRNAs targeting the 5 potential gene hits (i.e., *ACACA*, *LSS*, and *NDUFS1*, *NDUFA1, SDHB*) and 2 encompassed non-targeting sgRNAs, were mixed at an equal molar ratio for lentivirus production. SNU-1-Cas9 cells successfully transduced with the mini library at a MOI of ∼0.3, indicated by EGFP signal, were sorted out on day 5 post-infection. Within the same pool of sorted cells, genomic DNA was subsequently harvested from a subset of cells (2×10^5) the next day to serve as the initial time point, while another subset with the same cell number was maintained in regular 2D culture. For the remaining cells, 8×10^4 cells were subcutaneously injected into the right flank of each 6- to 8-week-old male NOD/SCID mouse (6 mice in total). At the end of the study, genomic DNA of the 2D-cultured cells and *in vivo* tumors were both harvested on day 35 post-infection. For the CRISPR screen with EN coculture, 4×10^7 single cells were used to transduce with the lentiviral library containing 1,412 sgRNAs targeting genes that were upregulated in ENS coculture at a MOI of ∼0.3 for 12-16 hrs. On day 7 post-infection, cells successfully transduced with the library, indicated by EGFP signal, were sorted out and split into a regular culture group and an indirect ENS coculture group. On day 14 post-infection, transduced cells from each group were treated with vehicle (DMSO) and RO 48-8071 (8 nM) for 7 days, respectively. After treatment, at least 8×10^5 cells were harvested for genomic DNA extraction to ensure over 500-fold coverage of the screening library.

Sample preparation for next-generation sequencing

Genomic DNA of the organoids was extracted by DNeasy Blood & Tissue Kit (QIAGEN). To amplify fragments containing sgRNA sequences in the first round PCR, 0.5 ng of library plasmid or 800 ng of genomic DNA was used as the template for each 50 μl PCR reaction using KAPA HiFi Hotstart Ready-mix (Kapa Biosystems). PCR cycles were optimized for each individual sample to minimize PCR bias by maintaining PCR amplification at the exponential phase. To ensure sufficient library coverage, 150 PCR reactions were performed for the genome-wide library screen, whereas 20 PCR reactions were required for other libraries in this study. The addition of Illumina adapters and sequencing indices to the amplicons was carried out in the second round of PCR. The final amplicons were purified using Agencourt AMPure XP beads (Beckman Coulter). Real-time PCR with SYBR® Premix Ex Taq™ (TaKaRa) was used to measure the quantity and quality of the PCR products. Samples were pooled and loaded on the Illumina NovaSeq 6000 system.

CRISPR screen data analysis

Raw read counts from the genome-wide library screen were processed using CRISPRcleanR.[80] Read counts were firstly normalised to the plasmid sample, the raw count of which less than 30 reads were excluded, for computing log fold-changes of sgRNAs using ccr.NormfoldChanges function. The output results were further processed to correct the biased sgRNAs' log fold changes with ccr.GWclean function on each individual chromosome. Corrected sgRNA counts derived from the corrected log fold-changes by ccr.correctCounts function were used as input for downstream analyses. To determine gene essentiality, gold-standard essential and non-essential reference gene sets were used to compute the BF and FDR for each gene in the genome-wide library using BAGEL[19] (Table S3). A gene with a higher BF indicates it is a fitness gene in GX117-T1O at higher confidence. The corrected sgRNA counts were also used as input into MAGeCK[18] v0.5.9 to identify depleted genes. -log RRA and log fold-changes were computed at the gene-level (Table S3). A high correlation between the BF and -log RRA indicates a high confidence in the fitness genes identified. Thus, MAGeCK and BAGEL calculate a Robust Rank Aggregation (RRA) score and a log Bayes factor (BF) score, respectively (all BF are log BF), for each gene. The more positive the $-\log_{10}$ (RRA) and BF scores indicate higher confidence that a given gene's knockout leads to a decrease in fitness. In our genome-wide CRISPR screen, 2,143 and 1,393 genes out of the initial population were depleted at a false discovery rate (FDR) cutoff of 5% and 1%, respectively (Figures 1B and 1C; Table S3). Pathway Enrichment Analysis revealed that known essential biological processes and cancer hallmarks, including Myc targets, E2F targets, and DNA repair, were enriched among these depleted genes (Figures S1C and S1D). The depleted genes also included *EGFR* and its signalling adaptors *GRB2* and *SOS1*, *FGFR2*, and *CTNNB1* (Table S3), which are important to support GX117-T1O's growth as its culture is maintained by supplementing EGF, FGF, and Wnt. The above results validate our technical framework for high-quality genome-wide CRISPR dropout screening in patient-derived tumor organoids. For the focused library CRISPR screen, raw read counts were input into BAGEL and MAGeCK. 28 essential and 28 non-essential genes strategically selected to be included in the library were used as the reference gene sets to ensure unbiased analysis. For the CRISPR screen with ENS coculture, statistical significance (Benjamini-Hochberg corrected) and normalized z scores for the RO-48-8071 screen were determined by DrugZ algorithm[83] to identify gene perturbations that enhance or suppress drug activity. sgRNA efficacy and gene essentiality were also determined using JACKS.[82] A gene with a higher NormZ score and higher JACKS score indicates it confers resistance to interaction with RO-48-8071.

Common essentials and GC-specific fitness genes

A list of pan-cancer core fitness genes identified as dependencies across all cell lines (CRISPR Inferred Common Essentials) was downloaded from the DepMap (23Q2). To define context-specific fitness genes for GC, gene dependency data of 33 GC cell lines were obtained from the DepMap as input for the ADaM in CoRe package[81] (https://github.com/DepMap-Analytics/CoRe/tree/master). A gene is classified as a fitness gene, especially to GC, when its significant fitness effect is exerted on more than 25 GC cell lines. With the removal of low-expressed genes ($\log_2$ TPM < -1), as well as the essential genes defined in both CRISPR Inferred Common Essentials and GC-specific fitness genes, 303 context-specific fitness genes of GX117-T1O with BAGEL FDR < 0.01 were identified. Among our pharmacologically validated hits (i.e., *ACACA* and *LSS* that are targeted by ND646 and RO 48-8071, respectively), *ACACA* and *LSS* are defined by DepMap as "strongly selective" genes whose dependency is observed in a subset of pan-cancer cell lines (i.e., at least 100 times more likely to have been sampled from a skewed distribution than a normal distribution[6]). Loss of fitness was observed in only 1.3% and 23.7% of the total 1,095 cell lines when *LSS* and *ACACA* were knocked out (Figure S3A). Similar percentages were also observed when considering only the GC cell lines (Figure S3A). *FASN* likewise showed "strongly selective" dependencies, with loss of fitness observed in 22.3% of cell lines (Figure S3A). LSS, ACC, and FASN could be the desired targets for further development of drugs with high efficacy and were thus included in our subsequent assays for evaluation. Considering only the GC cell lines used in the DepMap project, which lack the complex characteristics of organoids, most of these GC cell lines are also less sensitive to *LSS, ACACA*, and *FASN* knockouts (Figure S3A).

Analysis of Chronos data in organoid and GC cell lines

Post-Chronos gene effect scores of 33 GC cell lines downloaded from the DepMap and gene effects of GX117-T1O computed by Chronos[22] (https://github.com/broadinstitute/chronos) were batch-corrected with the Combat function using the sva package (v3.34.0) for gene essentiality distribution comparison (Figure S1F). A gene with a score of 0 represents it is not essential, while -1 represents it is an essential gene.

Target tractability

Prioritization of potential drug targets was assessed by the tractability of small molecules or antibodies documented in the Open Targets platform (22.04) (https://platform.opentargets.org/downloads).[25,26] The genes were categorized into 10 tractability bins (with Bin 1 indicating the highest tractability). Tractability group 1 (Bin 1-3) contains targets with approved drugs or compounds in clinical or preclinical phases, while tractability group 2 (Bin 4-7) consists of targets without drugs in clinical use but with experimental evidence of molecules binding and thus represent good candidates for further validation and therapeutic development. Targets with uncertain or no evidence of molecules binding are grouped in group 3 (Bin 8-10).

Pathway enrichment analysis

Genes of interest were queried against the Molecular Signatures Database (MSigDB) using ShinyGO 0.76[85] or the Gene Set Enrichment Analysis (GSEA) website (https://www.gsea-msigdb.org/gsea/msigdb). Significantly enriched pathways with FDR < 0.05 were selected.

Flow cytometric analysis and cell sorting

To prepare samples for flow cytometry, organoids and cells were dissociated by TrypLE or Trypsin (Gibco) respectively, then resuspended in FACS buffer (PBS with 2% FBS) and filtered through a 70-μm strainer (Corning). ACEA NovoCyte Quanteon (Agilent) was used to detect the signal of EGFP by 488 nm blue laser (530/30 nm), BFP by 405 nm violet laser (445/45 nm) or mCherry by 561 nm yellow-green laser (615/20 nm). For cell sorting, organoids or cells were prepared in a similar approach as in flow cytometry, but resuspended with FACS buffer supplemented with 2X P/S or antibiotic-antimycotic, respectively. Fluorescent cells detected by their respective lasers were sorted by a CytoFlex SRT cell sorter (Beckman Coulter) equipped with 100-μm nozzle in Purity sort mode. Sorted organoids or cells were collected and cultured in a medium supplemented with 2X P/S or antibiotic-antimycotic, respectively, which was replaced with fresh culture medium on the next day.

Drug validation assay

Drugs used in this study were purchased from Cayman, except that RO 48-8071 and 5-FU were obtained from MedChemExpress and Sigma-Aldrich, respectively. The optimal cell number for each line was seeded into 384-well or 96-well plates. An 8-point 2-fold dilution of drugs was performed using medium of a series of DMSO concentrations, the highest being 0.25%, as diluent was added one day after cell seeding, and the viability was quantified by Cell titer-Glo assay (Promega) using a microplate reader (Molecular Devices). Data was compared with a positive control treated with 10 μM MG-132 (Sigma-Aldrich) and a negative control with medium alone. IC_{50} values were generated according to the dose-response curves using gdsc IC_{50} R package.[96] Drug testing of GC organoids was performed as previously described[15,97] with slight modifications. ~15,000-20,000 organoids per ml were plated into each well of a 384-well plate coated with 50% BME using a Multidrop Combi Reagent Dispenser (Thermo Fisher). The drug was treated on the next day, and the viability was quantified on day 6. Drug testing in cell lines was performed as previously described[98] with slight modifications. 2,000 - 4,000 cells were seeded into each well of a regular 96-well plate (2D), an ultra-low binding 96-well plate (to form 3D spheroids), or a 96-well plate with 50% BME gel coating (to form organoid-like structures), using a Multidrop Combi Reagent Dispenser. The drug was administered on the next day, and the viability was quantified at a 72-hr time point. To determine the rescue effect of exogenous fatty acids in ND646 treatment, the cell seeding procedure for organoids and cell lines is the same as above. ND646 was treated the next day, with BSA control (Cayman, 29556) and 50-100μM palmitate (Cayman, 29558) or oleate (Cayman, 29557) supplemented as appropriate. The same procedures also apply to drug assays with ENS coculture, except that organoids were seeded using 50% complete medium and 50% ENS-conditioned medium. In the validation experiment for the CRISPR screen with ENS coculture, Cas9-expressing organoids were infected with lentivirus of the desired sgRNAs at 70-80% infection rate. On day 7 post-infection, cells successfully transduced with the sgRNA, indicated by EGFP signal, were sorted out and cultured under indirect ENS coculture. On day 14 post-infection, transduced cells were dissociated. ~15,000-20,000 organoids per ml were seeded into each well of a 384-well plate coated with 50% BME. Organoids were treated with RO 48-8071 the next day, and their viability was assessed on day 6 post-treatment. The same procedure was applied to the drug assay with acetylcholine, acetate, and ENS secretome molecules treatment, with organoids cultured with complete medium supplemented with corresponding concentrations of acetylcholine (Merck, A2661), acetate (Millipore, 567422), serotonin hydrochloride (MedChemExpress, HY-B1473), GABA (MedChemExpress, HY-N0067), dopamine hydrochloride (MedChemExpress, HY-B0451A), VIP, (MedChemExpress, HY-P1023), neuropeptide Y (MedChemExpress, HY-P1601), substance P (MedChemExpress, HY-P0201), and TNF-α (MedChemExpress, HY-P1860). For the ENS secretome experiment, the molecules were administered in three different dosage combinations: low, mid, and high. These dosages were from previous studies and scaled up or down for use in the current study. The ENS secretome molecules included in the combination consisted of serotonin hydrochloride[99] (low: 0.1 μM; Mid: 10 μM; High: 20 μM), GABA[100] (low: 0.1 μM; Mid: 10 μM; High: 20 μM), dopamine hydrochloride[101] (low: 0.1 μM; Mid: 10 μM; High: 20 μM), VIP[102] (low: 0.1 μM; Mid: 1 μM; High: 2 μM), neuropeptide Y[103] (low: 10 nM; Mid: 100 nM; High: 200 nM); substance P[104] (low: 10 nM; Mid: 100 nM; High: 200 nM) and TNF-α[105] (low: 20 ng/ml; Mid: 40 ng/ml; High: 80 ng/ml).

Growth competition assay

Cas9-expressing organoids were infected with lentivirus of the desired sgRNAs, aiming for 70-80% infection rate. EGFP was quantified by flow cytometry on day 7 or day 14 post-infection as appropriate, and was measured every 7 days. A similar approach was

performed in cell lines. To allow enough room for competition, an extra step of mixing the EGFP$^+$ cells with uninfected cells 3 days after infection was required to decrease the proportion of the EGFP$^+$ population if the infection rate was over 90%. EGFP was quantified by flow cytometry on day 7 post-infection and was measured every 3 days as cells proliferate faster than organoids. Data was first normalized with the safe harbor at each time point, followed by normalization with the initial time point.

DNA editing efficiency

Cas9-expressing organoids were established by pAWp63-clone32 transduction, followed by 2 weeks of zeocin (400 μg/ml) selection. 2-4 weeks were required for organoids to recover from the selection. Cas9 activity was confirmed by measuring the percentage of EGFP depletion with pAWp9-1 (Addgene, 73852) transduction, normalized against the positive control transduced with pAWp9 (Addgene, 73851). GFP knockout efficiency (%) = (100% - GFP knockout gRNA% / Total infected cells %) * infection rate. To determine the indel percentage at the selected endogenous loci, Cas9-expressing organoids were infected with lentivirus of the desired sgRNAs. Successfully transduced organoids were sorted out on day 12-14 post-infection, indicated by EGFP signal. Genomic DNA of the sorted organoid was extracted by QuickExtract™ DNA Extraction Solution (Bioresearch Technologies), followed by amplification of the interested sgRNA region. Purified PCR fragments were sent for Sanger sequencing, and the indel results were analysed by Inference of CRISPR Edits (ICE).[106]

GFP transfer assay

GFP-based Touching Nexus[45] was used to determine the cell-cell interaction between organoids and ENCCs under coculture conditions. pLVX-RT003-GPM (Addgene, 163383) and pLVX-RT004-LaG30VB (Addgene, 163384) were gifts from Monte Winslow. Organoids and ENCCs were transduced with lentivirus of the desired plasmids at 80-90% infection rate. Infected cells were sorted out based on their BFP, GFP, and mCherry signals using flow cytometry. Surface GFP ligand-expressing (sGFP) sender cells and cell surface anti-GFP nanobody-expressing (αGFP) receiver cells were seeded in a 24-well ultra-low binding plate at high seeding density. GFP transfer was quantified every 2 days. Cells were dissociated with TrypLE and analyzed by flow cytometry.

Immunocytochemistry

Differentiated ENs and EN coculture with GC organoids were fixed with 4% PFA at room temperature overnight and rinsed three times with PBS. Cells were then permeabilized by PBS containing 0.2% Tween-20 for 15 min and blocked by PBS containing 1% BSA and 2% glycine for 1 hr. Cells were then incubated with primary antibodies (TUJ1, R&D Systems, MAB1195, 1:1,000; TrkC, Cell Signaling, 3376, 1:1,000; MAP2, Cell Signaling, 4542, 1:1,000) for enteric neuron-specific markers overnight at 4°C with gentle shaking. After shaking, cells were incubated with goat Alexa Fluor 488/568-conjugated anti-mouse/rabbit IgG secondary antibodies (Thermo Fisher, A-11001, A-11011, 1:1,000) at room temperature for 1 hr in the dark. Nuclei were counterstained with DAPI (Invitrogen). Enteric neuron identity was confirmed by immunofluorescence photomicrographs captured under a fluorescence microscope.

Western blot

Cells were dissociated into single cells and rinsed with PBS. Protein extracts were prepared by homogenizing the cell pellet with cell lysis buffer supplemented with protease and phosphatase inhibitors. Total protein concentration was determined by the Bradford assay. Equal amounts of total protein (10-30 μg) were separated on SDS-PAGE gels and transferred to PVDF membranes, followed by blocking with 5% milk or BSA as appropriate at room temperature for 1 hr and incubation with primary antibodies including ACC1 (Cell Signalling, 4190S, 1:1,000), SREBP1 (Abcam, ab28481, 1:1,000), GAPDH (Cell Signalling, 2118S, 1:1,000), MLKL (Abcam, ab184718, 1:1,000), phospho-MLKL (Abcam, ab187091, 1:1000) and ARHGAP26 (Atlas Antibody, HPA035107, 1:500), overnight at 4 °C with gentle shaking. Upon washing, the membrane was probed with HRP-conjugated goat anti-rabbit antibody (Cell Signalling, 7074S, 1:5,000) for 1 hr and visualized with Pierce ECL Western Blotting substrate (Thermo Scientific).

Free fatty acid and triglyceride assays

HGC-27-Cas9 cells infected with lentivirus of the dummy- or *ACACA*-sgRNA were harvested on day 21 post-infection. *In vivo* tumors with dummy or *ACACA* knockouts were cut and weighed. Cellular free fatty acid and triglyceride concentrations were measured using the Free Fatty Acid Quantification Assay Kit (Abcam) and Triglyceride Quantification Assay Kit (Abcam) according to manufacturer's protocol, respectively. Concentrations detected in tumor tissues were normalized against their respective weights. Based on the assumption that 1 g of tumor weight equals 1 x 10^8 cells,[107] the number of cells within the tumor was estimated to enable fair comparisons with *in vitro* samples using the equivalent number of cells.

Metabolomics analysis

Frozen cell pellets of 2D-cultured SNU-1-Cas9 cells, GX117-T1O and 50 mg tumors with dummy or *ACACA* knockouts, each group of which contained an estimated cell number of 5 x 10^6,[107] were subjected to non-polar and polar metabolite detection and analysis. Frozen pellets containing the same number of SNU-1-Cas9 cells cultured with ultra-low binding plates or BME coating were subjected to non-polar metabolite detection and analysis. For polar metabolite analysis, an additional step was performed where the cell pellet was resuspended in 2 ml 80% methanol with 200 ng Norvaline internal standard after sample collection. Samples were analyzed by Agilent 7890B GC - Agilent 7010 Triple Quadrapole Mass Spectrometer system for GC-MS/MS analysis at the Centre

for PanorOmic Sciences at The University of Hong Kong. Data analysis was performed by the Agilent MassHunter Workstation Quantitative Analysis Software (version B.07.01).

Clinical data set

The Cancer Genome Atlas (TCGA) – Stomach adenocarcinoma (STAD) clinical data, including overall survival, progression-free survival, and disease-specific survival, were obtained from the PanCancer Atlas at cBioPortal (https://www.cbioportal.org/). Gene expression levels of *LSS* and *ACACA* for the respective patients were downloaded from the UCSC Xena (https://xena.ucsc.edu/).

Gene knockout study in mice

5 x 10^4 SNU-1-Cas9 cells infected with a dummy sgRNA or a sgRNA targeting *ACACA* or *LSS* gene were resuspended in 100 μl BME. The resulting cell suspensions were then subcutaneously injected into the left and right flank of each 6- to 8-week-old male NOD/SCID mouse, respectively, 4 days after sgRNA infection. A similar approach was applied to HGC-27-derived xenograft mice. 2 x 10^5 HGC-27-Cas9 cells infected with the desired sgRNAs were subcutaneously injected into the right flank of each 6- to 8-week-old male BALB/cAnN-nu mouse. Tumor volumes were measured every 4 days using an electronic caliper and calculated by the following equation: length (mm) x width^2 (mm) x 0.5. The mice were sacrificed on day 44-48 post-injection, and the collected tumor tissues were snap-frozen and stored at -80°C for downstream experiments. Cas9-expressing organoids were first infected with lentivirus containing pHIV-Luc-ZsGreen (Addgene, 39196), followed by enriching the successfully transduced organoids with a cell sorter. EGFP$^+$ organoids were infected with lentivirus carrying BFP-dummy sgRNA or BFP-sgRNAs targeting *ACACA* or *LSS*, aiming for an over 90% infection rate. 1 x 10^6 sgRNA-infected organoids were resuspended with 100 μl BME on day 4 post-infection and were injected intraperitoneally into 6- to 8-week-old male BALB/cAnN-nu mice. The mice were monitored every 5 days using bioluminescence imaging with the IVIS® Spectrum imaging system upon luciferin administration, starting from week 2-3 post-injection. Luminescent intensity of photons emitted from the tumor was quantified using Living Image® Software (Caliper Life Sciences).

Drug response study in mice

For ND646 drug treatment, 1 x 10^5 SNU-1 cells in 100 μl BME were subcutaneously injected into the right flank of each 6- to 8-week-old male BALB/cAnN-nu mouse. Tumor growth was monitored every 3 days. Mice were randomly assigned to the vehicle or the treatment group when tumor volumes reached ~100 mm^3. Vehicle solution (0.9% saline, 5% Tween 80, 40% PEG 400) or ND646 (12.5 mg/kg) was administered orally twice a day for 24 days. For RO 48-8071 drug treatment, 2 x 10^5 HGC-27 cells were subcutaneously injected into the right flank of each 6- to 8-week-old male NOD/SCID mouse. Vehicle solution (0.9% saline, 5% Tween 80, 40% PEG 400) or RO 48-8071 (40 mg/kg) was given to mice intraperitoneally once per day for 24 days. The dosages reported were primarily decided based on the results of our pilot experiments to determine the highest safe dose for ND646[31] and RO 48-8071,[108] as well as from a literature search. Tumor growth was monitored every 4 days. At the end of the study, mice received a final dose 1 hour prior to euthanasia and tumor collection.

RNA-sequencing

RNA-seq experiments were performed at the Centre for PanorOmic Sciences, The University of Hong Kong. For the gene expression level that serves as the threshold for gene hit selection and correlation, RNA was extracted, and the $\log_2$ TPM was generated as previously described.[15,16] RNA extraction from tumor organoids and 2D-cultured cell suspensions, as well as *in vivo* tumors, was performed using the MiniBEST Universal RNA Extraction Kit (TaKaRa) in accordance with the manufacturer's instructions. Qualified RNA samples accessed by Qubit Fluorometer (Invitrogen) and Bioanalyzer 2100 (Agilent) were proceeded using KAPA mRNA HyperPrep Kit (Kapa Biosystems) to prepare for the cDNA library, which was then sequenced with Illumina NovaSeq 6000. The sequence reads were aligned to the reference human genome (hg19) using the Rsubread package. Only genes with > 0.5 counts-per-million in at least half of the samples were included in the differential expression analysis, which was performed using edgeR and limma packages.

For the gene expression comparison between a panel of GC organoids and cell lines, the expression level of organoids was obtained from the patient-derived GC organoid biobank dataset,[15] whereas the GC cell lines' expression level was downloaded from the Cancer Cell Line Encyclopedia (2019v) (Methods S2). Only genes with > 0.5 counts-per-million in at least 10 samples were included in the differential expression analysis. The gene raw counts were compared between GC organoids and cell lines by limma analysis to obtain the DEG list (p-value < 0.01) for downstream pathway enrichment analysis.

Splicing analysis

RNA of GX058-TO control and its respective *CTNND1-ARHGAP26* knockout clone was extracted. RNA of GX058-TO with *MAGOHB* knockout and its corresponding control were extracted using the same procedures mentioned above. Raw RNA-seq reads of tumor organoid controls and knockout samples were first aligned against the human reference genome (GRCh38) with GENCODE v44 gene annotations using STAR[89] (version 2.7.11b) under default parameters. In-frame fusion transcripts with fusion fragments per million total RNA-seq fragments (FFPM) > 0.1 were retrieved by STAR-Fusion[90] (version 1.7.0). Splice junctions and chimeric read alignments identified were then processed using Trinity Cancer Transcriptome Analysis Toolkit (CTAT)-splicing (version 0.0.3) for the detection of introns resulting from potential aberrant splicing. Alternative splicing events, including alternative

3' splice sites, alternative 5' splice sites, mutually exclusive exons, retained introns, and exon skipping, were detected by rMATS[91] (version 4.1.1). Differential alternative splicing events between tumor organoid controls and their respective knockout samples were determined, followed by downstream pathway enrichment analysis.

QUANTIFICATION AND STATISTICAL ANALYSIS

Results were expressed as mean ± standard deviation (SD). Biological replicates (n number) were specified for each experiment in the figure legends. If not otherwise specified, statistical analyses were performed by Prism 9 (GraphPad) using Student's t-test for the comparison between two groups, as well as one-way or two-way ANOVA with post hoc test stated for the comparisons among multiple groups. SPSS v25 (IBM) was used for the pairwise comparison. p-value < 0.05 was used and considered statistically significant unless stated otherwise.